

# Quantum Interference Line Shifts of Broad Dipole-Allowed Transitions

Thomas Udem,\* Lothar Maisenbacher, Arthur Matveev, Vitaly Andreev, Alexey Grinin, Axel Beyer, Nikolai Kolachevsky, Randolph Pohl, Dylan C. Yost, and Theodor W. Hänsch

High-resolution laser spectroscopy serves the purpose of determining the energy difference between states of atoms and molecules with the best possible accuracy. Therefore, one may face the problem of finding the center of a symmetric line within a small fraction of the line width, or one needs to extract the energy difference from an asymmetric line without a uniquely defined center. Multiplets of atomic resonance lines are subject to mutual line pullings and give rise to asymmetric line distortions due to quantum interference. This paper reviews the treatment of these distortions for dipole-allowed one-photon transitions. Specific examples are given for hydrogen and helium spectroscopy.

$m_e$ . In that case, the Rydberg constant  $R_\infty = \alpha^2 m_e c / 2h$  will only have fixed non-dimensionless constants and one dimensionless constant, the fine structure constant  $\alpha$ . Unfortunately, the fine structure constant cannot be calculated yet, despite interesting speculations.<sup>[4]</sup> All atomic and molecular energy levels are given by the Rydberg constant that multiplies a dimensionless theoretical expression. Due to its simplicity, that theoretical expression is best known for atomic hydrogen and hence a “computable clock” would make use of this system.

## 1. Introduction

Precise experimental values for energy levels in atomic and molecular systems are needed for testing fundamental physics, comparing atomic clocks and for realizing the new International System of Units (SI).<sup>[1]</sup> The latter has no more artifacts. It defines most of the units by fixing non-dimensionless constants and thereby removing real objects (natural or artificial) from the definitions. With the new SI, the only remaining reference to an existing object is to the Cs atom, or more precisely to the difference between its ground state hyperfine energy levels. The line splitting, that is, the uncertainty of energy difference in units of line width has reached parts in  $10^6$ . Any other unit (except for the mole) now hinges on this transition.<sup>[2]</sup>

The next amendment of the SI will most likely be the replacement of the Cs transition with an optical transition to represent the second.<sup>[3]</sup> In the future, it may even be conceivable to relate the SI second to a computable atomic transition by fixing one final non-dimensionless constant, say the mass of the electron

An essential tool for this endeavour is precision spectroscopy to measure or represent the difference between energy levels that is not necessarily the center of the observed line. Besides fixing or determining constants, the test of quantum electrodynamics (QED) calculations requires precision spectroscopy as well. In that case however, two or more independent measurements are required to check for consistency.<sup>[5]</sup> Since there is only one metrologically relevant narrow line in atomic hydrogen (the 1S–2S transition), one has to determine the transition energy from a typical MHz wide line to within an uncertainty at the kHz level. This is a severe challenge that sets the current limit on testing QED and determining the values of natural constants such as the charge radius of the proton.<sup>[6]</sup>

Quite similar, the fine structure constant may be determined from the measurement of the electron  $g$  factor if one believes in QED calculations of this dimensionless constant.<sup>[7]</sup> To test QED, one needs at least one more independent measurement of the fine structure constant, say by determining atomic recoil<sup>[8,9]</sup> or by measuring difference of energy levels in helium.<sup>[10–13]</sup> Again, a wide line width transition has to be analyzed.

The purpose of this contribution is to review quantum interference (also referred to as cross damping) as a commonly observed but often ignored line distortion that may occur in high-resolution laser spectroscopy, in particular when analyzing wider lines. This effect has first been described by F. Low in 1952 in order to analyze the natural line shape for the determination of the Lamb shift.<sup>[14]</sup> In this work, we summarize our work on atomic hydrogen; however, we keep the derivations general, so that it can be readily applied to any other atom. In contrast to earlier works (see, e.g., ref. [15]), we use perturbation theory (see, e.g., ref. [16]). This approach has the advantage of producing analytic line shape functions that can be fitted to experimental data, but can not easily be used to include saturation or pumping phenomena as well as temporally modulated excitation such as the Ramsey scheme.

Prof. T. Udem, L. Maisenbacher, Dr. A. Matveev, V. Andreev, A. Grinin, Dr. A. Beyer, Prof. D. C. Yost, Prof. T. W. Hänsch  
Max-Planck-Institut für Quantenoptik  
Hans-Kopfermann Str. 1, 85748 Garching, Germany  
E-mail: thomas.udem@mpq.mpg.de

Dr. N. Kolachevsky  
P.N. Lebedev Physical Institute  
Leninsky prospekt 53, 119991 Moscow, Russia  
Prof. R. Pohl  
Johannes Gutenberg-Universität Mainz, Institut für Physik  
QUANTUM und PRISMA+, 55128 Mainz, Germany

The ORCID identification number(s) for the author(s) of this article can be found under <https://doi.org/10.1002/andp.201900044>

DOI: 10.1002/andp.201900044

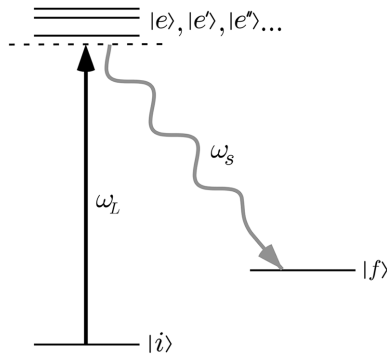


**Figure 1.** Connecting a particular initial state  $|i\rangle$  to a particular final state  $|f\rangle$  via indistinguishable paths leads to interference. The laser excitation takes place with the frequency  $\omega_L$  that is detuned (dashed line) relative to the excited states  $|e\rangle, |e'\rangle, |e''\rangle \dots$ . In general, the emitted frequency  $\omega_s$  is different from the impinging laser frequency unless the initial and final states are identical, in which case the situation resembles a colocated ensemble of classical driven oscillators.

The level scheme considered here is the one sketched in **Figure 1**. It starts from an initial state  $|i\rangle$  that is laser excited to  $|e\rangle$  with subsequent decay to a final state  $|f\rangle$ . This process can lead to interference if (and only if) there are several possible paths, that is, several excited states  $|e\rangle, |e'\rangle, |e''\rangle \dots$ . This interference phenomenon can lead to line distortion. Note that the initial and final states do not have to be different states.

## 2. Classical Toy Model

If the initial and final states are identical, that is,  $|i\rangle = |f\rangle$ , the system behaves more intuitively as a collection of colocated classical oscillating dipoles. These dipoles are in forced oscillation driven by the exciting laser and hence all vibrate at the laser frequency, that is,  $\omega_L = \omega_s$ . The phase and amplitude response is given by their susceptibility. In this description, the interference takes place in the emitted fields instead of between transition paths within the atom.

For simplicity, we limit the discussion within the classical toy model to two phased dipole emitters that have resonance frequencies  $\omega_0$  and  $\omega_1 = \omega_0 + \Delta$ . We are interested in describing the “line pulling” that the main resonance at  $\omega_0$  experiences due to the presence of a far-detuned resonance at  $\omega_1$  (see **Figure 2**). By line pulling, we mean that the center of the line no longer coincides with the transition energy. In particular, we are discussing asymmetric line distortions that leave the line center as a matter of definition. For simplicity, we assume for now that both resonances have the same damping constant  $\Gamma$ . The orientation of the driven dipoles are given by the vectors  $\vec{D}_0$  and  $\vec{D}_1$  that do not need to be parallel. They add up to the total dipole moment  $\vec{D}(\omega_L)$ . Within this toy model, we do not care how the dipoles  $\vec{D}_0$  and  $\vec{D}_1$  are generated. This will be addressed in the quantum mechanical treatment in Section 3. With the usual susceptibilities, the total dipole moment is given by:

$$\vec{D}(\omega_L) \propto \frac{\vec{D}_0}{(\omega_L - \omega_0) + i\Gamma/2} + \frac{\vec{D}_1}{(\omega_L - \omega_0 - \Delta) + i\Gamma/2} \quad (1)$$

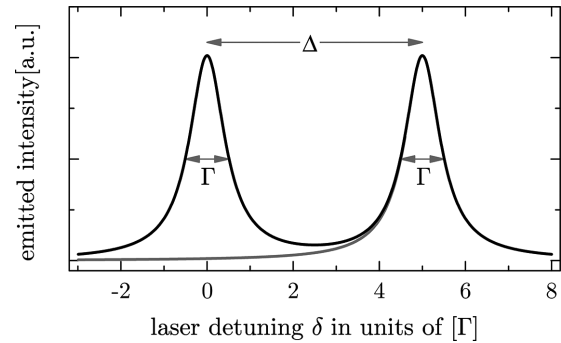


**Figure 2.** Sketch of the emission spectrum with two excited states. Excitation energies of the two transitions are  $\hbar\omega_0$  and  $\hbar(\omega_0 + \Delta)$ , in close proximity but not exactly equal to the peaks of the spectrum. For simplicity, we assume here identical widths  $\Gamma$  and identical dipole moments  $\vec{D}_0 = \vec{D}_1$ . The peak or center of the line of interest is pulled by the presence of the other line away from  $\omega_0$  in two ways: First (incoherently) because it sits on the sloping pedestal of the perturbing line (gray) and second (coherently) because of an intriguing interference effect that modifies the spatial emission pattern in a detuning dependent way. The same arguments can be made for the other line.

Placed at the origin, it generates a far-field electric field at position  $\vec{r}$  that is given by

$$\vec{E}(\vec{r}) \propto (\vec{r} \times \vec{D}(\omega_L)) \times \vec{r} \frac{e^{i\omega_L t - ik_L r}}{r^3} \quad (2)$$

such that the detected intensity, that is proportional to the square modulus of the field, is given by

$$I(\vec{r}, \omega_L) \propto \frac{r^2 |\vec{D}(\omega_L)|^2 - |\vec{D}(\omega_L) \cdot \vec{r}|^2}{r^4} \propto |\vec{D}(\omega_L)|^2 (1 - \cos(\beta))^2 \quad (3)$$

The last term expresses the dipole characteristic in terms of the angle  $\beta$  between  $\vec{D}(\omega_L)$  and  $\vec{r}$ . At this point, we do not care about the  $1/r^2$  roll-off of the total intensity with distance. Only the shape of the line should matter here. Since both, the amplitude and the direction of the total dipole  $\vec{D}(\omega_L)$  depends on the laser frequency, this angle varies as the laser is tuned over the resonances. Hence, for a fixed position of the detector we expect line distortions.

In the quantum mechanical treatment, the relative orientations between the dipoles is no longer a continuous variable. It will turn out, in this case, that the  $(1 - \cos(\beta))^2$  term does not depend on laser detuning. Therefore, we will also ignore this dependence for the toy model and assume that the observed spectrum is given by

$$|D(\omega_L)|^2 \propto \frac{D_0^2}{\delta^2 + (\Gamma/2)^2} + \frac{D_1^2}{(\delta - \Delta)^2 + (\Gamma/2)^2} + 2\vec{D}_0 \cdot \vec{D}_1 \frac{\delta(\delta - \Delta) + (\Gamma/2)^2}{(\delta^2 + (\Gamma/2)^2)((\delta - \Delta)^2 + (\Gamma/2)^2)} \quad (4)$$

Here, we have introduced the laser detuning  $\delta = \omega_L - \omega_0$  to highlight the symmetry of this expression.<sup>[17]</sup> Equation (4)

consists of two Lorentzians and a non-Lorentzian cross term. As we will see, the latter term vanishes relative to the two Lorentzians for  $\Gamma/\Delta \rightarrow 0$ . Therefore it is usually referred to as “cross damping” instead of “quantum interference” in this context. The cross term is often ignored when fitting experimentally obtained spectra. However, both the second and third terms will give rise to a systematic error of the main lines energy difference (first term) if an incomplete fitting function is used. The second term takes into account that the main resonance sits on the pedestal of the perturbing resonance, which appears as an approximately linear background. We call this incoherent line pulling, because it can also be obtained by simply adding the intensities of the two lines. The last term is due to interference between the emissions of the two components and hence we refer to it as coherent line pulling.

### 2.1. Large Line Separation

For a sufficiently large spectral separation of the two resonances ( $\Delta \gg \Gamma$ ), the full line shape can be expanded around the resonance of interest, that is, for  $\delta \ll \Delta$ .<sup>[18]</sup> Therefore, the first term in (4) is treated as the main resonance and the other terms are expanded. For the second term, we find an approximately linear background with

$$\frac{D_1^2}{\Delta^2 + (\Gamma/2)^2} + \frac{2D_1^2\Delta}{(\Delta^2 + (\Gamma/2)^2)^2} \delta + \dots \approx \frac{D_1^2}{\Delta^2} + \frac{2D_1^2}{\Delta^3} \delta \quad (5)$$

For the third term in (4), we keep the Lorentzian factor and expand the remainder around  $\delta \approx 0$ :

$$\begin{aligned} & \frac{2\bar{D}_0 \cdot \bar{D}_1}{\delta^2 + (\Gamma/2)^2} \left( \frac{(\Gamma/2)^2}{\Delta^2 + (\Gamma/2)^2} - \frac{\Delta(\Delta^2 - (\Gamma/2)^2)}{(\Delta^2 + (\Gamma/2)^2)^2} \delta + \dots \right) \\ & \approx \frac{2\bar{D}_0 \cdot \bar{D}_1}{\delta^2 + (\Gamma/2)^2} \left( \frac{(\Gamma/2)^2}{\Delta^2} - \frac{\delta}{\Delta} \right) \end{aligned} \quad (6)$$

In total, we get for the main component plus corrections in first order:

$$|D(\omega_L)|^2 \propto \frac{a_1}{\delta^2 + (\Gamma/2)^2} + a_2 \delta + a_3 + a_4 \frac{\delta}{\delta^2 + (\Gamma/2)^2} \quad (7)$$

with

$$\begin{aligned} a_1 & \approx D_0^2 + 2\bar{D}_0 \cdot \bar{D}_1 \frac{\Gamma^2}{4\Delta^2}, & a_2 & \approx \frac{2D_1^2}{\Delta^3}, \\ a_3 & \approx \frac{D_1^2}{\Delta^2}, & a_4 & \approx -\frac{2\bar{D}_0 \cdot \bar{D}_1}{\Delta} \end{aligned} \quad (8)$$

where again  $\Delta \gg \Gamma$  has been used. The third term in (7) can be dropped because it is a constant, that is, independent of  $\delta$  and hence does not pull the line, and for the analysis of experimental data, a constant offset is usually already included as a background in the line shape. The first term is the unperturbed main resonance around  $\delta = 0$  and  $a_2$  and  $a_4$  are asymmetric corrections that pull the main line if not properly taken into account.

Note that the symmetric line distortions would not pose a serious problem if one is interested in finding the line center only. For this, it would be sufficient to fit almost any other symmetric line shape.

It turns out that many asymmetric line distortions can be modeled by adding a small dispersive term like the last one in (7). The usefulness of this expansion lies in the fact that the full and complicated geometry dependence of the fourth term is described by only one coefficient  $a_4$  and the line distortions add linearly scaled with  $a_4$  to the unperturbed line shape. That is, summing up over different emission and detection positions only changes  $a_4$ , but not the shape of the distortion itself. The same line shape is maintained in the quantum mechanical treatment, albeit with different explicit expressions for  $a_1 \dots a_4$  (see Section 3.6). In practice, they will be used as fitting parameters anyway. Additional perturbing peaks in the spectrum do not lead to additional terms. They will merely change the values of the parameters  $a_1$  through  $a_4$ . This is because as long as the perturbing resonances are sufficiently far detuned, their spectral behavior at the resonance of interest is independent of their lifetime (i.e., the Lorentzian pedestals always look like  $1/\omega_L^2$  for large detuning).

The  $a_2$  coefficient is due to the incoherent line pulling of the main line sitting on the pedestal (linearly expanded) of the perturbing line at  $\delta = \Delta$ . The  $a_4$  coefficient describes the coherent effect of cross damping. To investigate their relative importance, we first need to agree upon the way the line pulling is quantified. Because the line is not simply shifted but also distorted, different parts of the line are shifted by different amounts. We will define the line pulling as the displacement of the half-width points of the main line around  $\delta = 0$  which gives:<sup>[18]</sup>

$$\Delta\omega = \frac{2a_4\Gamma^2 + a_2\Gamma^4}{8a_1} \quad (9)$$

$$\approx \frac{2a_4\Gamma^2 + a_2\Gamma^4}{8D_0^2} \left( 1 - \frac{\bar{D}_0 \cdot \bar{D}_1}{2D_0^2} \frac{\Gamma^2}{\Delta^2} + \dots \right) \quad (10)$$

$$\approx -\frac{\bar{D}_0 \cdot \bar{D}_1}{2D_0^2} \frac{\Gamma^2}{\Delta} + \frac{(\bar{D}_0 \cdot \bar{D}_1)^2 + D_0^2 D_1^2}{4D_0^4} \frac{\Gamma^4}{\Delta^3} + \dots \quad (11)$$

The leading term in the expansion in powers of  $\Gamma/\Delta$  is the leading term of  $a_4/a_1$  whereas the incoherent pulling  $a_2$  is suppressed by  $\propto (\Gamma/\Delta)^2$ . In most cases, it can be ignored. In fact, it will even partially be compensated when fitting line shapes with the parameters  $a_1$  and  $a_4$  only. To place an upper limit on the order of magnitude of the line pulling, one might assume equal and parallel dipole moments. In that case, the line pulling is expected to be  $\Delta\omega \approx \Gamma^2/2\Delta$ . This rule of thumb has also been obtained by M. Horbatsch and E.A. Hessels<sup>[15]</sup> using the optical Bloch equations.

Alternatively, one might define the line pulling as the shift of the maximum of the main line. It turns out that this reduces the leading term in (11) by a factor two.<sup>[18]</sup> Both of these definitions work for theoretical expressions but not for real experimental data that is subject to noise. In that case, a more reasonable strategy is to first fit a Lorentzian, that is, the slightly wrong line shape to average over the noise and then use its peak to quantify the line pulling. It turns out that this method essentially gives the leading term in (11), with a slight dependence on the frequency

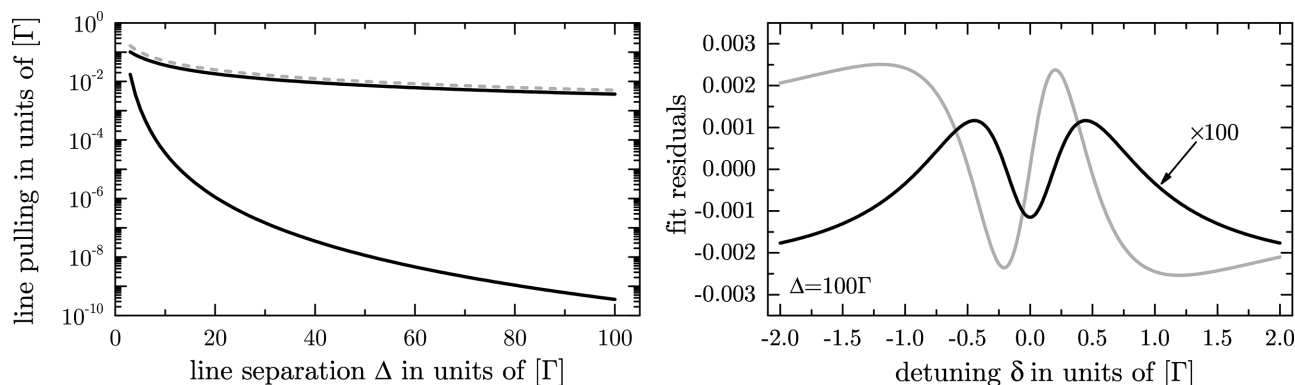


**Figure 3.** Left: Line pulling obtained when line distortions due to cross damping (quantum interference) are not properly taken into account. To quantify and correct this error, samples are generated using the full line shape model given by (4) with identical and parallel dipole moments  $\vec{D}_0 = \vec{D}_1$  and identical line widths  $\Gamma$ . By fitting two Lorentzians within a frequency range of  $\omega_L = (\omega_0 - 2\Gamma, \omega_0 + 2\Gamma)$ , the upper black curve is obtained that measures the line pulling as a function of line separation (both in units of  $\Gamma$ ). Very similar curves are obtained when fitting with the first and second term in (7). On the other hand fitting with the first and last term of (7) reduces this error by many orders of magnitude (lower black curve). The gray dashed curve shows the “rule of thumb” value  $\Delta\omega \approx \Gamma^2/2\Delta$ . Right: Fit residuals of the peak normalized line shape (4) with  $\Delta = 100\Gamma$  fitted with the approximate line shape (7) without the linear and dispersive term ( $a_2 = a_4 = 0$ , black) and without only the linear term ( $a_2 = 0$ , gray). It can be seen that including the dispersive contribution reduces the residuals by two orders and, even more importantly, symmetrizes the remaining residuals. Therefore, the line pulling is removed to a large extent.

range used for fitting. This is not a surprise because fitting is most sensitive to the points with the largest slope. Residual deviations of the model can always be determined by generating artificial data according to the full line shape (4), and employing the *same* wrong function for fitting. This is investigated in Figure 3.

## 2.2. Related Effects

There are several other problems in atomic physics related to cross damping. One of them is connected with the widely spread rotating wave approximation, that is, neglecting the negative frequency of an exciting radio frequency or laser field that goes along with a real-valued driving force. In this sense, even a pure two-level system gives rise to two resonances that are mirror images about  $\omega = 0$ . Just like the cross-damping pulling, ignoring the negative frequency component leads to an error that is actually not a shift but is rather due to using an incomplete line shape model. Nevertheless, this problem has been called the Bloch–Siegert shift.<sup>[19]</sup> With the formalism above, we can compute this “shift” by choosing the perturbing line to be the negative component with  $\Delta = -2\omega_0$ , and amplitudes  $\vec{D}_1 \cdot \vec{D}_2 = -1$ ,  $D_1^2 = 1$  to  $\Delta\omega = \Gamma^2/4\omega_0$ . The usual textbook expression given for spin magnetic resonances is  $\Delta\omega_{BS} = \Omega^2/4\omega_0$ ,<sup>[19]</sup> where  $\Omega$  is the Rabi frequency. While magnetic resonances have essentially  $\Gamma \approx 0$ , for optical transitions in the perturbation regime, we have  $\Omega \approx 0$ . In the intermediate case, we would have a power broadened line with  $\Gamma' = \sqrt{\Gamma^2 + 2\Omega^2}$  (see ref. [20], Equations (2.24b) and (2.27b)). Therefore, we replace  $\Gamma$  by  $\sqrt{2}\Omega$  in the expression for the line pulling. The usual textbook expression for the Bloch–Siegert shift for spin magnetic resonances is then describing the shift of the peak, while the leading term in (11) predicts it to be twice as large. Because of the large line separation, the Bloch–Siegert is hardly ever relevant for optical transitions.

Another related phenomenon is quantum beats,<sup>[21]</sup> that is a temporal modulation of the emitted light from atoms that have

been initialized to two excited states at the same time. This excitation is done with a short laser pulse whose spectrum covers both transitions from an initial state. After the pulse, the classical analogue corresponds to freely decaying oscillators rather than forced oscillators. In that case, the frequency  $\omega_L$  in (1) is no longer the driving frequency but the Fourier frequency of the emitted radiation. The latter consists of two components such that a beat note is observed in the time domain. The cross term in (4) acquires a time dependence whose frequency corresponds to the energy difference of the contributing excited states and the phase is given by the initial conditions, that is, a short pulse excitation (see ref. [21] for details).

Similarly, several laser frequencies might be present at the same time to drive a single transition. In the extreme case, one might use a frequency comb with typically  $10^5$  equidistant laser frequencies. The observed spectrum is periodic with the mode spacing or pulse repetition rate. Therefore, one might expect that these lines give rise to cross damping as described before. However, when driving a dipole-allowed single-photon transition in this way,<sup>[22]</sup> the emissions that belong to the various laser modes take place at different laser frequencies. The cross terms are therefore beating at the mode spacing frequency, typically on the order of 100 MHz. A photodetector that receives the fluorescence typically has a much lower bandwidth such that the cross terms average out quickly. This situation is very similar for two-photon comb spectroscopy, even though the classical toy model may not be best to describe this situation. In this case, many pairs of modes add up to the same transition frequency. The ones that do not, belong to off-resonant excitation. However, in both cases, (comb driven single-photon and two-photon) additional line components are present so that the cross damping effect, as discussed before, enters. The treatment for the two-photon case is somewhat more involved and requires third-order perturbation instead of second order or the solution of the proper optical Bloch equations. Details for the hydrogen 1S–3S transition are presented in ref. [23,24].

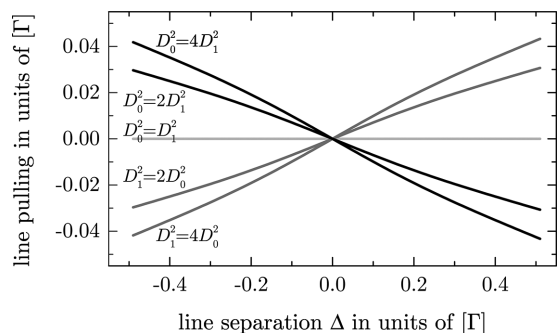


**Figure 4.** In the spirit of fitting the “wrong” line shape to determine the corrections required and subsequently fix the error, we first generate artificial line profiles with (4). These line shapes are then fitted with the same profile but dropping the cross term. The plot shows the line pulling as a function of line separation  $\Delta$ .

Another related phenomenon is the line profile frequently observed in photoelectron spectroscopy. Here, direct ionization and ionization via a doubly excited autoionizing state are two quantum paths that connect common initial and final states. In this context, the line shape is a Fano profile. In fact, expanding the Fano line shape given in ref. [25], and keeping only terms first order in the Fano parameter, results in the same line shape as (7).

### 2.3. Unresolved Lines

Another important situation occurs when the interfering lines are not well resolved<sup>[16]</sup> as in Figure 2 but instead  $\Delta \ll \Gamma$ . This might take place, for example, if the hyperfine structure is buried within the natural line width. The 2S–8D transition in atomic hydrogen<sup>[26]</sup> is an example. In this case, the emitted spectrum appears in first order as a single line with a slightly larger line width. There seems to be little hope that the main transition energy can be extracted with a large line splitting factor unless the line separation  $\Delta$  is very well known. This is often the case if the buried line components are due to the hyperfine structure.

Taking advantage of this knowledge one can use the full line shape (4) with a fixed value of  $\Delta$  instead of an approximate line shape (7). In practice though, the main issue will be that the relative intensities of the terms in (4) will not be exactly as theory predicts. Tiny variations of the relative intensities will have a severe effect of the center of mass on the resulting convoluted line. The relative strength of the first two terms may depend on the laser polarization. Likewise, the relative intensity of the cross term depends on the detector position, the solid angle of detection, polarization, sensitivity, etc. These parameters are difficult to control with good accuracy. One can solve this problem by introducing two adjustable parameters that rescale the second and third term of (4). Fitting this line shape in this way does not introduce an error in the sense of a known deviation between the fitted and the observed function.

To investigate the influence of the cross damping term in this case, we fit the line shape using (4) but dropping the cross term. **Figure 4** shows the result for different relative intensities  $D_0^2/D_1^2$ . It can be seen that neglecting cross damping gives errors intolerable for precision experiments, except for the case where the

two lines occur with the same intensity ( $D_0^2 = D_1^2$ ). In the latter case, the residuals are symmetric about the line center  $\delta = \Delta/2$  and hence no line pulling occurs, even when the fit does not describe the line shape well. However, with the arguments above, it is probably not advisable to assume exactly equal intensities, even if theory predicts that.

A similar situation occurs for single peaks that are split through the Zeeman effect or when the transition is observed in a standing wave to suppress the first-order Doppler effect.<sup>[27]</sup> Depending on the magnitude of these splittings and the accuracy goal, one may ignore or fit the full line shape, as described before, to compensate.

### 2.4. Simultaneous Separated and Unresolved Lines

Well-separated and unresolved line components may occur simultaneously, for example, with unresolved hyperfine structure and well-resolved fine structure. Again, the 2S–8D transition in atomic hydrogen<sup>[26]</sup> is an example because the 2S–8S transition is also allowed through a two-photon excitation. To derive a suitable line shape model for this situation, we start with an expression analogous to (1), but with three dipole moments  $\vec{D}_0$ ,  $\vec{D}_1$ , and  $\vec{D}_2$ . The transition energy of the first two is assumed to be separated by small detuning  $\Delta_< \ll \Gamma$  that is not resolved, while the third resonance is well resolved and detuned by  $\Delta_> \gg \Gamma$  from the first one. Computing the spectral intensity as in (4) leaves us with three real-valued Lorentzians and three cross terms. Two of the latter correspond to large detunings and may be expanded as in (7) while the third one may be treated as in the previous section assuming an a priori knowledge of  $\Delta_<$ . The total line shape will then look like:

$$|D(\omega_L)|^2 \propto \frac{b_1}{\delta^2 + (\Gamma/2)^2} + \frac{b_2}{(\delta - \Delta_<)^2 + (\Gamma/2)^2} + \frac{b_3\delta(\delta - \Delta_<) + (\Gamma/2)^2}{((\delta^2 + (\Gamma/2)^2)((\delta - \Delta_<)^2 + (\Gamma/2)^2))} + b_4\delta + b_5\frac{\delta}{\delta^2 + (\Gamma/2)^2} + b_6\frac{\delta - \Delta_<}{(\delta - \Delta_<)^2 + (\Gamma/2)^2} \quad (12)$$

Here,  $b_1 \dots b_6$  are adjustable parameters. A constant term  $\propto \Delta_<$  has been dropped like in (7). For real-world noisy data, fitting this function works remarkably well, because the contributions from the separated lines and the unresolved lines are quite different in shape about the line center.

### 2.5. Doppler Broadening

So far the treatment has been for single atoms at rest. In a real experiment, one often deals with many atoms that are in motion, for example, in a gas or in an atomic beam, and we have to include the velocity distribution. The frequency *shift* may be cancelled by some Doppler-insensitive method like saturation spectroscopy, two-photon spectroscopy, or by employing a standing wave (see, e.g., ref. [28,29]). To model the remaining Doppler *broadening*, we assume the atoms to be spatially distributed in a random fashion

so that their contributions to the emitted field do not have fixed phase relations. This means that the emitted intensity (4) rather than the emitted field (1) has to be convolved with the velocity distribution. In other words, the different Doppler components do not cross damp. With regard to Horbatsch/Hessels' rule of thumb that was mentioned in the wake of (11), a good limit for the line pulling is to replace the natural line width with the observed line width.

In the case of well-separated lines (Section 2.1), we convolve the expanded line shape (7) with a Gaussian (Maxwellian velocity) with a full width at half maximum of  $\Gamma_G$ . While ignoring the second term, the convolution of the first and the last term can be cast into the real and imaginary part of the Faddeeva function<sup>[6,30]</sup> (also known as the complex error function  $w(z)$ )<sup>[31]</sup>. For computational reasons, it is advantageous to rewrite the convoluted profiles in terms of these standard functions for which fast and precise algorithms exist:<sup>[32]</sup>

$$|D(\omega_L)|^2 \propto A \left( \text{Re}[w(z)] + 2\eta \text{Im}[w(z)] \right) \quad \text{with} \\ z = 2\sqrt{\ln(2)} \left( \frac{\delta}{\Gamma_G} + i \frac{\Gamma}{2\Gamma_G} \right) \quad (13)$$

This fit function, we call the Fano–Voigt line shape, was used for the data analysis in [6]. It involves six free parameters, the center frequency  $\omega_0$ , the amplitude  $A$ , a constant background, the Lorentzian and Gaussian widths,  $\Gamma$  and  $\Gamma_G = \omega_0 \sqrt{2k_B T / Mc^2}$  (FWHM in rad s<sup>-1</sup>) and the asymmetry parameter  $\eta = a_4 \Gamma / 4a_1$  (see (7)).

Folding the cross term in (4) with a Gaussian can be done in a similar way resulting in

$$|D(\omega_L)|^2 \propto A \left( \text{Re}[w(z)] + \xi \text{Re} \left[ (2 + i2\Delta/\Gamma)w(z) \right. \right. \\ \left. \left. + (2 - i2\Delta/\Gamma)w(z - \Delta/\Gamma_G) \right] \right) \quad (14)$$

with another adjustable parameter  $\xi$  and the same definition of  $z$ . To convolve the line shape (12), one has to add (13) and (14) with two additional parameters.

### 3. Quantum Mechanical Treatment

While the classical toy model gives some intuition into the problem, it is incomplete as it does not provide the dipole moments of individual oscillators. In addition, it fails in some cases when the initial and final states are not identical. For example, exciting the  $2S(F=0) \rightarrow 4P_{1/2}(F=1)$  transition in atomic hydrogen with linearly polarized light (only  $F=0 \rightarrow F=1$  allowed) and observing the photons emitted upon the decay to all the  $1S$  Zeeman levels, we find a spherical symmetric emission pattern (see coefficient  $a_1$  in (46)). This is not in agreement with the expected emission pattern of a classical dipole. We are not aware of a classical analogue that takes discrete energy levels properly into account. This problem shows up in full when all three, the initial, excited, and final levels are different.

#### 3.1. Optical Bloch Equations with Cross Damping

There are two approaches that deal with cross damping within the realm of quantum mechanics. The more fundamental one starts from the master equation for the interaction of a multi-level atomic system with a quantized electromagnetic field using the density matrix formalism and uses the Wigner–Weisskopf approximation to treat spontaneous decay as a result of the interaction with the electromagnetic vacuum.<sup>[33,34]</sup> With this procedure a Liouville–von Neumann equation

$$\frac{\partial \rho}{\partial t} = \frac{1}{i\hbar} [\hat{H}, \rho] - \hat{\mathcal{L}}\rho \quad (15)$$

is obtained where the atomic part and the coherent atom–light interaction are given by

$$\hat{H} = \sum_n |n\rangle \langle n| \hbar\omega_n + \frac{\hbar}{2} \sum_j (\hat{S}_j^+ \Omega_j e^{i\omega_L t} + \hat{S}_j^- \Omega_j^* e^{-i\omega_L t}) \quad (16)$$

The first sum runs over all levels with energy  $\hbar\omega_n$  with one of them typically chosen to be zero while the second sum runs over all transitions that are connected by the coherent laser field at frequency  $\omega_L$ . The Rabi frequencies  $\Omega_j = d_j E / \hbar$  are given by the electric field of the laser and the dipole matrix element  $d_j$  of the transition  $j$ . In some cases, it is advantageous to work with a complex Rabi frequency, that is, a complex field to readily include phase shifts such as the ones caused by the Doppler effect (with  $E = E_0 e^{-i\vec{k}\cdot\vec{r}}$ ). The projection operators  $\hat{S}_j^+$  are given by terms like  $|i\rangle \langle e|$  for all transitions that are connected by the coherent laser field. Likewise, the conjugate operators  $\hat{S}_j^-$  are given by terms like  $|e\rangle \langle i|$ .

Spontaneous emission is described by the Lindblad operator:

$$\hat{\mathcal{L}}\rho = \frac{1}{2} \sum_{ij} \Gamma_{ij} \{ \hat{S}_i^+ \hat{S}_j^- \rho - 2\hat{S}_j^- \rho \hat{S}_i^+ + \rho \hat{S}_i^+ \hat{S}_j^- \} \quad (17)$$

Again the indices  $i$  and  $j$  do label transitions not levels, but spontaneous transitions in this case. The so-called cross damping decay constants are given by  $\Gamma_{ij} = \sqrt{\Gamma_i \Gamma_j} \vec{\epsilon}_i \cdot \vec{\epsilon}_j$  where  $\Gamma_i$  and  $\Gamma_j$  are the decay constants for transition  $i$  and  $j$ , respectively. The spherical unit vectors along the corresponding dipole moment are given by  $\vec{\epsilon}_i$  (see below). The projection operators  $\hat{S}_j^+$  are now given by terms like  $|e\rangle \langle f|$  with the levels that correspond to the spontaneous decays  $i$ . Likewise the  $\hat{S}_j^-$  projectors are given by combinations like  $|f\rangle \langle e|$ . All other non-energy conserving terms disappear within the rotating wave approximation that is assumed here. Note that the final states may include some of the initial states. Cross damping occurs with  $i \neq j$  from at least two coherently populated excited states that decay with the same polarization, that is,  $\vec{\epsilon}_i = \vec{\epsilon}_j$  to a common final state.

Given all the projection operators, the transition energies and the decay constants, the optical Bloch equations are readily obtained from the Liouville–von Neumann Equation (15). See refs. [15,35,36] for examples of Bloch equations with cross-damping. With  $N$  levels, there are  $N^2$  real-valued differential equations. For large systems, a computer algebra system may be implemented that outputs these equations for subsequent numerical integration.

### 3.2. Perturbation Theory with Cross Damping

While numerical integration of the optical Bloch equations is an extremely powerful method that can include other effects like saturation, we will now focus on perturbation theory. This allows us to obtain analytic expressions for the line shapes. One may use the time evolution operator constructed from  $\hat{H}$  in a Dyson series to derive the Kramers–Heisenberg formula within the rotating wave approximation.<sup>[16,38]</sup> It uses the amplitude and phase of a classical electromagnetic wave at  $\omega_L$  scattered by an atom that is taken from the initial state  $|i\rangle$  to the final state  $|f\rangle$  via the excited state  $|e\rangle$  (see Figure 1):

$$S_{q,p}^{e,i \rightarrow f} \equiv \frac{d_p(i \rightarrow e) d_q(e \rightarrow f)}{\omega_L - \omega_{ei} + i\Gamma_e/2} \quad (18)$$

The energies of the involved levels are  $\omega_i, \omega_f$ , and  $\omega_e$  and the transition frequency is defined as  $\omega_{ei} = \omega_e - \omega_i$  while the frequency of the scattered wave is given by  $\omega_s = \omega_L - \omega_f + \omega_i$ . The inverse lifetime of the excited state is given by  $\Gamma_e$  while the lifetime of the final state does not enter. There are distinct absorption and emission dipole moments  $d_p(i \rightarrow e)$  and  $d_q(e \rightarrow f)$ , respectively. Their polarizations are given with spherical components  $p$  and  $q$  in order to apply the Wigner–Eckart theorem (see below). These components are related to the Cartesian components through

$$d_{-1} = +\frac{1}{\sqrt{2}}(d_x - id_y), \quad d_0 = d_z, \quad d_{+1} = -\frac{1}{\sqrt{2}}(d_x + id_y) \quad (19)$$

Analogous expressions hold for any other vector. The  $(q, p) = 0$  component represents a dipole moment that oscillates linearly along the  $z$ -axis ( $\pi$  component). By virtue of the  $\pm 90^\circ$  phase shift of the  $y$ -component relative to the  $x$ -component,  $(q, p) = \pm 1$  represent dipole moments that are circular about the  $z$ -axis, also called  $\sigma^\pm$  components. The correspondent light polarization depends on the propagation direction that the atom does not know about in the dipole approximation. These components are not only connected to polarizations but also to particular dipolar emission patterns (see below).

The scattering rate of a laser with electric field amplitude  $E_L$ :

$$R_{q,p}(i \rightarrow f) = \frac{\pi E_L^2 \omega_s^3}{\hbar^3 c^3 \epsilon_0} |D_{q,p}(\omega_L)|^2 \quad \text{with} \quad D_{q,p}(\omega_L) = \sum_e S_{q,p}^{e,i \rightarrow f} \quad (20)$$

describes the number of incident photons<sup>[39]</sup> with frequency  $\omega_L$  and polarization  $p$  that are converted to emitted photons with frequency  $\omega_s$  and polarization  $q$  while transferring the atom from  $|i\rangle$  to  $|f\rangle$ .

In this language, the cross damping effect seems to come in a different way from the optical Bloch equations but very similar to the classical counterpart (4). The coherent addition of all paths leading from the initial state via all possible excited states to the final state represent the distinct resonances and the cross terms that appear through the square modulus. Since the distinct quantum paths interfere, the phenomenon is often referred to as “quantum interference.” Finally, it should be noted that the initial and final states do not have to be identical, but they could be.

#### 3.2.1. Arbitrary Laser Polarization

For linear laser polarization along the  $z$ -axis or circular polarization about the  $z$ -axis, the scattering rate can be calculated with  $p = 0$  and  $p = \pm 1$ , respectively, using the above formalism. Any other polarization vector  $\vec{\epsilon}_L$  with spherical components  $\epsilon_p$  analogous to (19), has to be expressed in terms of a scalar product in order to decompose in spherical components of the dipole operator:

$$\vec{d}(i \rightarrow e) \cdot \vec{\epsilon}_L = \sum_p (-1)^p d_p(i \rightarrow e) \epsilon_{-p} \quad (21)$$

The absorbing dipole  $d_p(i \rightarrow e)$  in (18) has to be replaced with the sum on the right-hand side so that the total emitting dipole becomes:

$$D_{q,p}(\omega_L) = \sum_e \sum_p (-1)^p S_{q,p}^{e,i \rightarrow f} \epsilon_{-p} \quad (22)$$

For linear laser polarization along the direction  $(\theta_L, \varphi_L)$  for example, the polarization vector reads:

$$\epsilon_{-1} = +\frac{1}{\sqrt{2}}(\sin(\theta_L) \cos(\varphi_L) - i \sin(\theta_L) \sin(\varphi_L)) \quad (23)$$

$$\epsilon_0 = \cos(\theta_L) \quad (24)$$

$$\epsilon_{+1} = -\frac{1}{\sqrt{2}}(\sin(\theta_L) \cos(\varphi_L) + i \sin(\theta_L) \sin(\varphi_L)) \quad (25)$$

### 3.3. Matrix Elements

The Wigner–Eckart theorem (ref. [40], (4.120)) allows us to decompose the dipole matrix elements into a factor that contains the geometry (i.e.,  $z$ -components of the involved angular momenta) in the form of a 3j symbol, and a reduced matrix element that is independent of it:

$$\begin{aligned} \langle n, (IJ) FM | d_q | n', (I'J') F' M' \rangle \\ = (-1)^{F-M} \begin{pmatrix} F & 1 & F' \\ -M & q & M' \end{pmatrix} \langle n, (IJ) F || d || n', (I'J') F' \rangle \end{aligned} \quad (26)$$

In this expression, it is assumed that the nuclear angular momentum  $I$  and the total electronic angular momentum  $J$  are coupled to the total angular momentum of the atom  $F$  with  $z$ -component  $M$ . The principal quantum numbers of the involved electronic states are given by  $n$  and  $n'$ . The nuclear angular momentum is associated only with a magnetic dipole moment but not with an electric dipole moment. Therefore, the dipole operator does not act on  $I$ . In this situation, the reduced matrix elements can be further reduced (ref. [40], (4.175)):

$$\begin{aligned} \langle n, (IJ) F || d || n', (I'J') F' \rangle = (-1)^{I+J+F'+1} \sqrt{(2F+1)(2F'+1)} \\ \times \begin{Bmatrix} J & F & I \\ F' & J' & 1 \end{Bmatrix} \langle n, J || d || n', J' \rangle \end{aligned} \quad (27)$$

The total electronic angular momentum  $J$  is itself composed of two components, the total orbital angular momentum  $L$  and the total spin angular momentum  $S$  of the electrons. Again, the electric dipole operator does not act on spin so that the reduced matrix element reduces once more. In total, we get:

$$d_q(e \rightarrow f) = (-1)^{F_f - M_f} \begin{pmatrix} F_f & 1 & F_e \\ -M_f & q & M_e \end{pmatrix} \langle n_f, L_f || d || n_e, L_e \rangle$$

$$\times (-1)^{J_f + I + F_e + 1} \sqrt{(2F_f + 1)(2F_e + 1)} \begin{Bmatrix} J_f & F_f & I \\ F_e & J_e & 1 \end{Bmatrix}$$

$$\times (-1)^{L_f + S + J_e + 1} \sqrt{(2J_f + 1)(2J_e + 1)} \begin{Bmatrix} L_f & J_f & S \\ J_e & L_e & 1 \end{Bmatrix} \quad (28)$$

The last reduced matrix element  $\langle n, L || d || n', L' \rangle$  can be computed from any other line strength quantifier like oscillator strength or measured transition rates, etc.<sup>[41]</sup> For atomic hydrogen, the reduced matrix element can be computed analytically from (63.2) and (63.5) in ref. [42]. Here  $n_f, F_f, M_f, J_f$ , and  $L_f$  are the quantum numbers of the final state,  $n_e, F_e, M_e, J_e$ , and  $L_e$  are the quantum numbers of the excited state. An analogous expression for the absorbing dipole moment in (20) is obtained by replacing  $f \rightarrow e, e \rightarrow i$ , and  $q \rightarrow p$ . To analyze the line shape that belongs to the same  $n_e, L_e$  fine structure manifold, we set the reduced matrix element to 1 as it is a common factor to all Zeeman, fine, and hyperfine components. The 3j and 6j symbols may be computed using the Racah formula<sup>[43]</sup> or with dedicated computer routines. Both the 3j and 6j are given as square roots of (mostly small) integer ratios. Special cases, that should cover all practically relevant cases, are given in sections 4.2.2 and 4.2.4 of ref. [40].

### 3.4. Emitted Intensity Pattern

To compute the emitted pattern and spectrum, we now understand the scattering amplitude (18) in the following way: The energy denominator and the absorbing dipoles  $d_p(i \rightarrow e)$  determine the amplitude of the emitting dipole  $D(\omega_L)$  that is given in spherical components in (20). The far-field of the latter oscillating with frequency  $\omega_s$  and located at the origin can be described with classical electrodynamics (see (2)):

$$\vec{E}(\vec{r}) \propto (\vec{r} \times \vec{D}(\omega_L)) \times \vec{r} \frac{e^{i\omega_s t - ik_s r}}{r^3} \quad (29)$$

Here  $\vec{r}$  is the detection point and  $r = |\vec{r}|$  the distance from the origin. The latter is of no interest here so that the last factor in (29) is ignored. Only the direction in which the field is detected matters. This direction is described by  $(\theta, \varphi)$  in spherical coordinates<sup>[44]</sup> whose unit vectors are:

$$\vec{e}_r = \begin{pmatrix} \sin(\theta) \cos(\varphi) \\ \sin(\theta) \sin(\varphi) \\ \cos(\theta) \end{pmatrix}, \quad \vec{e}_\theta = \begin{pmatrix} \cos(\theta) \cos(\varphi) \\ \cos(\theta) \sin(\varphi) \\ -\sin(\theta) \end{pmatrix},$$

$$\vec{e}_\varphi = \begin{pmatrix} -\sin(\varphi) \\ \cos(\varphi) \\ 0 \end{pmatrix} \quad (30)$$

Plugging the spherical components  $\vec{D}(\omega_L)$ , given analogously to (19), into (29), yields an expression for the emitted field  $\vec{E}(\vec{r})$  for each spherical components  $q$  that might be used to verify that the field is transversal, that is,  $\vec{e}_r \cdot \vec{E}(\vec{r}) = 0$ . The expression for  $\vec{E}(\vec{r})$  is rather lengthy and not required, so it will not be reproduced here. Instead, the two polarization components along  $\vec{e}_\theta$  and  $\vec{e}_\varphi$  are of interest:

$$E_\theta(\theta, \varphi) \equiv \vec{e}_\theta \cdot \vec{E}(\vec{r}) \propto -\sin(\theta) D_{0,p}(\omega_L)$$

$$+ \frac{\cos(\theta)}{\sqrt{2}} \left( e^{+i\varphi} D_{-1,p}(\omega_L) - e^{-i\varphi} D_{+1,p}(\omega_L) \right) \quad (31)$$

$$E_\varphi(\theta, \varphi) \equiv \vec{e}_\varphi \cdot \vec{E}(\vec{r}) \propto \frac{i}{\sqrt{2}} \left( e^{+i\varphi} D_{-1,p}(\omega_L) + e^{-i\varphi} D_{+1,p}(\omega_L) \right) \quad (32)$$

The phase terms  $\exp(i\omega_s t - ik_s r)/r$  have been suppressed. To take the possibility of several final states into account, their intensities are added incoherently. This is because quantum paths that do not end at the same states do not interfere (see Figure 1). In total, we get for the intensity seen by a polarization insensitive detector,<sup>[45]</sup>

$$I(\theta, \varphi) \propto \left| \vec{e}_\theta \cdot \vec{E}(\vec{r}) \right|^2 + \left| \vec{e}_\varphi \cdot \vec{E}(\vec{r}) \right|^2$$

$$\propto \sum_f \left| \sum_{e,p} (-1)^p \left( -\sin(\theta) S_{0,p}^{e,i \rightarrow f} \right. \right.$$

$$\left. \left. + \frac{\cos(\theta)}{\sqrt{2}} \left( e^{+i\varphi} S_{-1,p}^{e,i \rightarrow f} - e^{-i\varphi} S_{+1,p}^{e,i \rightarrow f} \right) \right) \epsilon_{-p} \right|^2$$

$$+ \frac{1}{2} \sum_f \left| \sum_{e,p} (-1)^p \left( e^{+i\varphi} S_{-1,p}^{e,i \rightarrow f} + e^{-i\varphi} S_{+1,p}^{e,i \rightarrow f} \right) \epsilon_{-p} \right|^2 \quad (33)$$

where the dipole moment (22) together with (18) has been used. The sums over the excited states extend over all levels  $J_e, F_e, M_e$  that are close to resonance. The sum over the final states should extend over all levels  $J_f, F_f, M_f$  to which transitions are detected. This is the final expression for the single atom response that will be used to model all of the following line shapes. In some cases, it might be useful to separate the cross damping terms from the line shape. By adding the quantum paths via the excited states incoherently by pulling the sum over  $e$  out of the square modulus, one obtains the line shape without the cross damping. The difference to the total line shape gives the cross damping terms.

In many cases, laser excitation will take place with one of the standard polarizations  $\epsilon_p$  only. In that case, (33) can be further simplified

$$I_p(\theta) \propto \sin^2(\theta) \sum_f \left| \sum_e S_{0,p}^{e,i \rightarrow f} \right|^2$$

$$+ \frac{\cos^2(\theta) + 1}{2} \sum_f \left( \left| \sum_e S_{+1,p}^{e,i \rightarrow f} \right|^2 + \left| \sum_e S_{-1,p}^{e,i \rightarrow f} \right|^2 \right) \quad (34)$$

such that the three spherical components of the emitted light do not interfere. The emitted intensity is rotationally symmetric for each of the spherical components  $q$  and hence the  $\varphi$  dependence is dropped here. The first term is the  $\pi$  component ( $q = 0$ ) of the emitted radiation with its characteristic  $\sin^2(\theta)$  emission pattern, while the second term are the  $\sigma^\pm$  components ( $q = \pm 1$ ) that have identical intensity emission patterns. The relative intensities emitted along the positive  $z$ -axis ( $\theta = 0$ ) are (1,0,1) for the ( $\sigma^-$ ,  $\pi$ ,  $\sigma^+$ ) components because the  $\sum_f |\sum_e S_{q,p}^{e,i \rightarrow f}|^2$  are the same for all  $q$ . The intensities perpendicular to the  $z$ -axis ( $\theta = \pi/2$ ) are (1/2, 1, 1/2) with the same relative units. This means that the  $\pi$  component vanishes when observed along the  $z$ -axis while the  $\sigma$  components are only half as strong when observed perpendicular to the  $z$ -axis. In addition, one sees that all components contribute equally if the intensities along the  $x$ -,  $y$ -, and  $z$ -axes are added. However, the  $\sigma$  and  $\pi$  components can only be detected selectively with certain polarizations and/or detector positions.

To justify (34), let us investigate the selection rules expressed by the matrix elements (28). The terms appearing in (33) have the form  $\sum_{e,e'} S_{q,p}^{e,i \rightarrow f} (S_{q',p'}^{e',i \rightarrow f})^*$  and are proportional to the product of the following 3j symbols:

$$\begin{pmatrix} F_f & 1 & F_e \\ -M_f & q & M_e \end{pmatrix} \begin{pmatrix} F_e & 1 & F_i \\ -M_e & p & M_i \end{pmatrix} \begin{pmatrix} F_f & 1 & F_{e'} \\ -M_f & q' & M_{e'} \end{pmatrix} \begin{pmatrix} F_{e'} & 1 & F_i \\ -M_{e'} & p' & M_i \end{pmatrix}$$

Conservation of the  $z$ -component of the angular momentum requires that each of the 3j symbols vanish unless the sum of

$$\begin{aligned} & \sum_{L_f} \sum_{J_f, F_f} (2J_f + 1)(2F_f + 1) \underbrace{\begin{Bmatrix} L_f & J_f & S \\ J_e & L_e & 1 \end{Bmatrix} \begin{Bmatrix} L_f & J_f & S \\ J_{e'} & L_{e'} & 1 \end{Bmatrix} \begin{Bmatrix} J_f & F_f & I \\ F_e & J_e & 1 \end{Bmatrix} \begin{Bmatrix} J_f & F_f & I \\ F_{e'} & J_{e'} & 1 \end{Bmatrix}}_{= \delta_{L_e, L_{e'}} \delta_{J_e, J_{e'}}} \\ & \times \underbrace{\sqrt{(2F_e + 1)(2F_{e'} + 1)} \sum_{M_f, q} \begin{pmatrix} F_f & 1 & F_e \\ -M_f & q & M_e \end{pmatrix} \begin{pmatrix} F_f & 1 & F_{e'} \\ -M_f & q & M_{e'} \end{pmatrix}}_{= \delta_{F_e, F_{e'}} \delta_{M_e, M_{e'}}} \end{aligned} \quad (37)$$

the lower row vanishes. This means that  $M_f = q + M_e \wedge M_e = p + M_i \Rightarrow M_f = q + p + M_i$  and  $M_f = q' + M_{e'} \wedge M_{e'} = p + M_i \Rightarrow M_f = q' + p' + M_i$ . Subtracting the two resulting equations yields that only terms with  $q + p = q' + p'$  contribute to the sum and hence no mixing between the spherical components occurs, that is,  $q = q'$  if the sums over  $p$  and  $p'$  contain only one and the same  $p$ .

At last, it should be mentioned that both line shapes in this section, (33) and (34), may need to be convolved with a Gaussian to account for the velocity distribution as in Section 2.5.

### 3.5. Detection Solid Angle

The analysis so far assumes a point-like detector at a direction  $(\theta, \varphi)$  from the atom, which measures the line shape at this po-

sition via (33). A real detector though has a finite solid angle  $\Omega_d$  such that the received line shape becomes:

$$I(\Omega_d) = \iint_{\Omega_d} I(\theta, \varphi) \sin(\theta) d\theta d\varphi \quad (35)$$

An important limiting case is a detector that collects the total signal, that is,  $\Omega_d = 4\pi$  that may be difficult to reach in a real experimental set up. Integrating (34) yields

$$\begin{aligned} I(\Omega_d = 4\pi) & \propto \frac{8\pi}{3} \sum_f \left( \sum_{e,p} |(-1)^p S_{0,p}^{e,i \rightarrow f} \epsilon_{-p}|^2 \right. \\ & \left. + \sum_{e,p} |(-1)^p S_{-1,p}^{e,i \rightarrow f} \epsilon_{-p}|^2 + \sum_{e,p} |(-1)^p S_{+1,p}^{e,i \rightarrow f} \epsilon_{-p}|^2 \right) \\ & = \frac{8\pi}{3} \sum_{f,q} \sum_{e,p} |(-1)^p S_{q,p}^{e,i \rightarrow f} \epsilon_{-p}|^2 \end{aligned} \quad (36)$$

where the  $\sin(\theta) \cos(\theta)$  and  $\cos(2\varphi)$  cross terms have vanished upon integration in the first line. The remaining cross terms  $\sum_{f,q} S_{q,p}^{e,i \rightarrow f} (S_{q,p}^{e',i \rightarrow f})^*$  could give rise to the quantum interference. However, if the reduced matrix elements of all emitting dipole moments are identical, these cross terms also vanish for  $e \neq e'$  as can be seen by inspecting corresponding sums over the 3j and 6j symbols:

The resulting Kronecker deltas of the second factor are due to the orthogonality relation of the 3j symbols and are used in the first factor together with another orthogonality relation of the 6j symbols (summing over  $J_f$  and  $F_f$ ). Hence, quantum interference vanishes when detecting in  $\Omega_d = 4\pi$  unless at least two of the excited states have all identical angular momentum quantum numbers, and hence must differ in the principal quantum numbers. In this case, the reduced matrix elements are in general not identical. Typically, there will be no excited states whose energies are sufficiently close such that quantum interference is important. Exemptions require special level schemes and are discussed in the context of suppressing spontaneous emission.<sup>[36,37]</sup> For the application here, the important result is that there is no line distortion due to the quantum interference effect with a hypothetical  $4\pi$  detector that has no polarization sensitivity. This finding provides a guide to the design of the detector unit. A large detection

solid angle not only reduces possible systematic effects due to line distortion but also reduces the statistical uncertainty. This is a rare combination that should be exploited when possible (see detection unit in ref. [6] for example).

Intuitively, we can state that quantum interference gives rise to a detuning dependent variation of the spatial emission pattern. However, suppression of the emission in one direction is compensated by an enhanced emission into another direction. The Zeeman structure of at least one of the involved levels has to be taken into account to describe any directivity since at least one level must be  $L > 0$  for dipole transitions. Hence, a model that ignores the Zeeman structure, like a two-level system, cannot describe this behavior.<sup>[15]</sup>

A typical situation is that the detection solid angle is a cone with an opening angle  $\theta_c$  about the z-axis.<sup>[34]</sup> With the laser polarized linearly along the z-axis we find:

$$I_{p=0}(\Omega_d) = \int_0^{2\pi} \int_0^{\theta_c} I_p(\theta) \sin(\theta) d\theta d\varphi$$

$$\propto \frac{8\pi}{3} \sin^4\left(\frac{\theta_c}{2}\right) (2 + \cos(\theta_c)) \sum_f \left| \sum_e S_{0,p}^{e,i \rightarrow f} \right|^2$$

$$+ \frac{\pi}{12} (16 - 15 \cos(\theta_c) - \cos(3\theta_c))$$

$$\times \sum_f \left( \left| \sum_e S_{+1,p}^{e,i \rightarrow f} \right|^2 + \left| \sum_e S_{-1,p}^{e,i \rightarrow f} \right|^2 \right) \quad (38)$$

This expression reduces to (36) with  $\epsilon_{-p} = \delta_{p,0}$  for  $\theta_c = \pi$  and vanishes for  $\theta_c = 0$ . Explicit examples will be given in Section 4.

### 3.6. Expanding the Line Shape

As with the classical toy model (Section 2.1), we follow the analysis given by Jentschura and Mohr<sup>[18]</sup> for well-resolved lines and separate the sum over the resonances in (34) into the main perturbed resonance at  $\omega_{ei}$ , and the non-resonant perturbing resonances at  $\omega_{e'i}$ . Using (18), we get

$$\left| \sum_e S_{q,p}^{e,i \rightarrow f} \right|^2 = \frac{d_p^2(i \rightarrow e) d_q^2(e \rightarrow f)}{\delta^2 + (\Gamma_e/2)^2}$$

$$+ \delta \sum_{e' \neq e} \sum_{e'' \neq e} \frac{d_p(i \rightarrow e') d_q(e' \rightarrow f) d_p(i \rightarrow e'') d_q(e'' \rightarrow f)}{(\omega_{e'} - \omega_e)^2 (\omega_{e''} - \omega_e)^2}$$

$$\times (\omega_{e'} + \omega_{e''} - 2\omega_e)$$

$$- 2\delta \frac{d_p(i \rightarrow e) d_q(e \rightarrow f)}{\delta^2 + (\Gamma_e/2)^2} \sum_{e' \neq e} \frac{d_p(i \rightarrow e') d_q(e' \rightarrow f)}{\omega_{e'} - \omega_e} \quad (39)$$

where we have reintroduced the laser detuning from the main resonance  $\delta = \omega_L - \omega_{ei}$  and neglected the damping term  $\Gamma_{e'}$  for the non-resonant terms. Note that the matrix elements  $d_q$  are real. In comparison with (9) in ref. [18], we have left out the counter-rotating terms ( $B_i^*(\epsilon_L, \epsilon_s)$  in their notation), that is, neglected the

Bloch–Siegert shift. Analogous to (7), the emitted intensity of (34) is written as:

$$I_p(\theta, \varphi) \propto \frac{a_1}{\delta^2 + (\Gamma/2)^2} + a_2 \delta + a_4 \frac{\delta}{\delta^2 + (\Gamma/2)^2} \quad (40)$$

with

$$a_1 = d_p^2(i \rightarrow e) \sum_f \left[ \sin^2(\theta) d_0^2(e \rightarrow f) + \frac{\cos^2(\theta) + 1}{2} \right.$$

$$\left. \times (d_{-1}^2(e \rightarrow f) + d_{+1}^2(e \rightarrow f)) \right] \quad (41)$$

$$a_2 = \sum_f \sum_{e' \neq e} \sum_{e'' \neq e} \frac{d_p(i \rightarrow e') d_p(i \rightarrow e'') (\omega_{e'} + \omega_{e''} - 2\omega_e)}{(\omega_{e'} - \omega_e)^2 (\omega_{e''} - \omega_e)^2}$$

$$\times \left[ \sin^2(\theta) d_0(e' \rightarrow f) d_0(e'' \rightarrow f) \right.$$

$$+ \frac{\cos^2(\theta) + 1}{2} (d_{-1}(e' \rightarrow f) d_{-1}(e'' \rightarrow f)$$

$$+ d_{+1}(e' \rightarrow f) d_{+1}(e'' \rightarrow f)) \left. \right] \quad (42)$$

$$a_4 = -2 \sum_f d_p(i \rightarrow e) \sum_{e' \neq e} \frac{d_p(i \rightarrow e')}{\omega_{e'} - \omega_e}$$

$$\times \left[ \sin^2(\theta) d_0(e \rightarrow f) d_0(e' \rightarrow f) \right.$$

$$+ \frac{\cos^2(\theta) + 1}{2} (d_{-1}(e \rightarrow f) d_{-1}(e' \rightarrow f)$$

$$+ d_{+1}(e \rightarrow f) d_{+1}(e' \rightarrow f)) \left. \right] \quad (43)$$

analogous to the classical toy model (8). With these coefficients the line pulling can be computed using (9) with the leading order  $a_4 \Gamma^2 / 4a_1$ . Although the sums look rather frightening in the general case, they actually do not have many terms in most cases. For example, if there is only one perturbing transition, the sums over  $e'$  and  $e''$  have only one term. In addition the squares of the 3j and 6j symbols in (28) are small fractions. With a computer algebra system an analytic expression for the general case is readily obtained. Unresolved lines can be treated in an analogous way (see Sections 2.3 and 2.4). A possible Doppler width can be folded into (40) as described in Section 2.5.

## 4. Explicit Examples

### 4.1. The Lamb Shift

Probably the most prominent example in precision spectroscopy, that requires one to find the energy difference of two levels by investigating a broad line, is the Lamb shift. This is a splitting between the 2S and the 2P<sub>1/2</sub> levels in atomic hydrogen that is not predicted by the Dirac theory but by QED. In the context

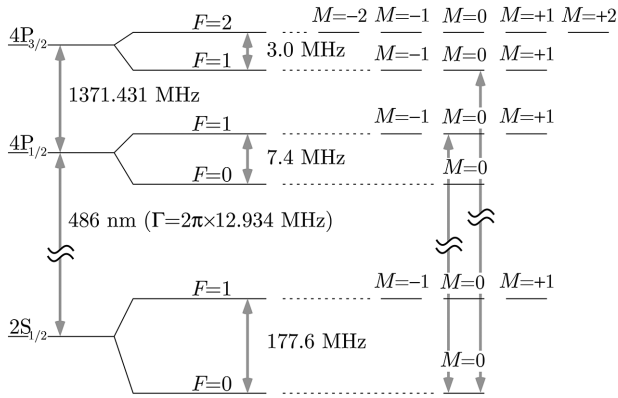


**Figure 5.** Level scheme of the hydrogen 2S–4P multiplet with nuclear spin  $I = 1/2$ . Left: The fine structure splitting of the 4P state is around 1.4 GHz while the hyperfine splittings are 7.4 and 3.0 MHz. Right: Preparing the atoms in the 2S ( $F = 0$ ) state, there are only two allowed Zeeman components with a laser linearly polarized along the z-axis. These components are spectrally separated by about 1.4 GHz, that is,  $\Delta/\Gamma \approx 100$ , so that quantum interference terms should be taken into account if one wants to find the line center to better than  $\sim 1\%$  (means approximately) of the line width.<sup>[15]</sup>

of this work, one would expect that the 2S–2P<sub>1/2</sub> transition at about 1 GHz is perturbed by the 2S–2P<sub>3/2</sub> transition at about 10 GHz, since these lines are only separated by about 100 line widths ( $\Gamma_e = 2\pi \times 100$  MHz). Line pullings of the MHz order would be the result,<sup>[14]</sup> whereas kHz uncertainties are required for modern QED tests.<sup>[46]</sup> Fortunately, the effect of quantum interference is insignificant in the Ramsey excitation scheme where the detected signal is not the emitted light but the surviving 2S atoms.<sup>[47]</sup> Provided that all Zeeman sublevels are detected with the same efficiency, no quantum interference is expected because this situation is analogous to a detection solid angle of  $4\pi$ .

## 4.2. The Hydrogen 2S–4P Transition

In contrast, quantum interference may be important for the hydrogen 2S–4P transition that played a decisive role in illuminating the so-called “proton radius puzzle,” a discrepancy between precision laser spectroscopy on regular hydrogen and muonic hydrogen.<sup>[48]</sup> The proton charge radius, together with the Rydberg constant, enters the theoretical description of the energy levels of atomic hydrogen. By measuring at least two energy differences, one can obtain values for these constants. Unfortunately, there is only one metrologically relevant transition<sup>[49]</sup> with a narrow line width—the 1S–2S transition with a natural line width of 1.3 Hz. All of the other useful transitions have several 100 kHz or even several MHz natural line widths. Therefore, at least one energy difference has to be obtained from a broad line, which then sets a limit on the accuracy of the proton charge radius and the Rydberg constant. As described in ref. [28], we chose to repeat the measurement of the 2S–4P transition<sup>[6]</sup> and improve previous results.<sup>[50]</sup> **Figure 5** shows the scheme of the involved levels.

In our experiment a cold beam of 2S atoms is generated with laser excitation at 243 nm from the ground state, which prepares the initial metastable 2S ( $F = 0$ ) state. After exciting the

2S–4P transition with a second laser at 486 nm, the atoms decay to the 1S state (final state). In previous experiments the standard detection method has been to observe the number of surviving 2S atoms.<sup>[50]</sup> This method does not suffer from line distortions due to quantum interference as long as all 2S Zeeman sublevels are detected with the same efficiency. However, with this detection method one needs to measure a small dip on a large noisy background. Therefore, we decided to detect fluorescence instead and deal with the quantum interference. Two resonances, the 2S ( $F = 0$ )  $\rightarrow$  4P<sub>1/2</sub> ( $F = 1$ ) and the 2S ( $F = 0$ )  $\rightarrow$  4P<sub>3/2</sub> ( $F = 1$ ) contribute with an intensity ratio of 1:2. They are spectrally separated by  $\Delta = 2\pi \times 1367$  MHz and have identical line widths of  $\Gamma \equiv \Gamma_e = 2\pi \times 12.9$  MHz. The toy model (11) predicts the 2S ( $F = 0$ )  $\rightarrow$  4P<sub>1/2</sub> ( $F = 1$ ) line to be pulled by up to  $\Gamma^2/\sqrt{2}\Delta \approx 2\pi \times 86$  kHz if quantum interference is ignored and a point-like detector is used. Since an uncertainty of the order of 1 kHz is required to be relevant to the proton radius puzzle, this must be taken into account in our experiment.

### 4.2.1. Full Line Shape

To derive the full line shape, we take as the initial state the 2S state with  $F_i = M_i = 0$ ,  $J_i = 1/2$ , and  $L_i = 0$ . Further, we assume the laser that drives the 2S–4P transitions to be linearly polarized along the z-axis ( $p = 0$ ) and use (34) with the reduced matrix elements in (28) set to unity. The 4P excited states are  $F_{e'} = 1$ ,  $M_{e'} = 0$ ,  $J_{e'} = 1/2$ ,  $L_{e'} = 1$ , and  $F_{e''} = 1$ ,  $M_{e''} = 0$ ,  $J_{e''} = 3/2$ ,  $L_{e''} = 1$  (see **Figure 5**). Detection is assumed to take place in the direction ( $\theta, \varphi = 0$ ) via the 4P–1S decay channel such that  $J_f = 1/2$ ,  $L_f = 0$ , and  $F_f = 1, 0$  (with all allowed  $M_f$ ). This yields the explicit full line shape function of this transition<sup>[51]</sup>

$$I^{P_{1/2}}(\theta) \propto \left| \frac{1}{\delta + i\Gamma/2} - \frac{1}{\delta - \Delta + i\Gamma/2} \right|^2 (1 + \cos^2(\theta)) + \left| \frac{1}{\delta + i\Gamma/2} + \frac{2}{\delta - \Delta + i\Gamma/2} \right|^2 \sin^2(\theta) \quad (44)$$

where we set the unperturbed 2S–4P<sub>1/2</sub>  $J_e = 1/2$  resonance to  $\delta = 0$ . For any other linear laser polarization, one could pick the z-axis to align along the laser polarization. Alternatively, one can use (33) for linear polarization along ( $\theta_L, \varphi_L = 0$ ) to obtain the same line shape except that  $\theta$  is replaced by  $\theta - \theta_L$ . The Zeeman sublevels  $M_e = -1, 0, +1$  that need to be summed over in this case are assumed to be degenerate, that is, representing a single energy denominator in (18) per excited state. A more complicated expression for non-vanishing  $\varphi_L$  could be given, but does not lead to new insights, because the coordinate system can always be chosen such that  $\varphi_L = 0$ . This line shape for linearly polarized excitation and perpendicular detection is plotted in **Figure 6** together with a Lorentzian fit that, at first glance, seems appropriate, even for the noise-less theoretical curve. However, the fit residuals at the bottom reveal the problem. Line distortions are almost fully asymmetric and hence most effective for line pulling effects.

It is instructive to compute the intensity emitted into each of the spherical components separately, even though they cannot be easily measured separately. For this purpose, we subtract the direct resonances  $\sum_e |S_{q,p}^{e,i \rightarrow f}|^2$  from the corresponding sums in

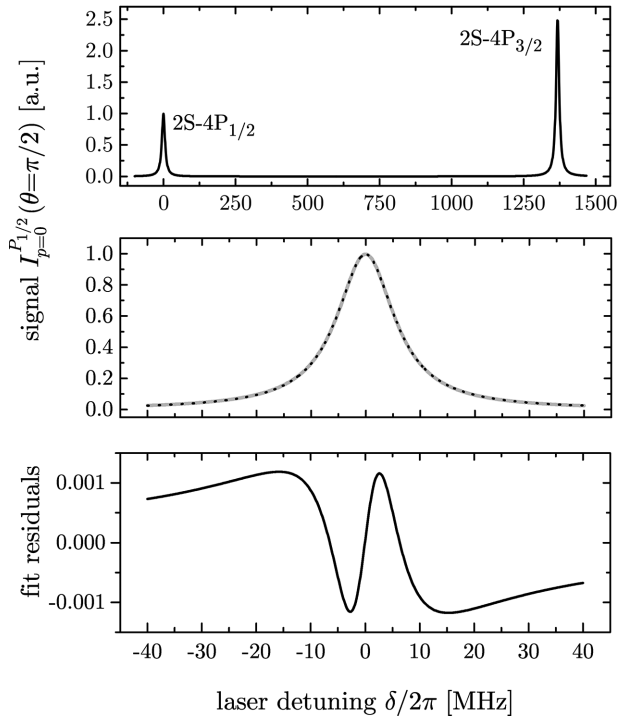


**Figure 6.** Top: The hydrogen 2S–4P<sub>1/2</sub> and 2S–4P<sub>3/2</sub> resonance excited with linear  $p = 0$  laser polarization (along z-axis) when detecting all fluorescence, that is, independent of polarization, along the x-axis ( $\theta = \pi/2$ ,  $\varphi = 0$ ) according to the full line shape model of (44). Zero detuning is chosen to be the non-perturbed 2S–4P<sub>1/2</sub> resonance. Only one hyperfine component,  $F = 0 \rightarrow F = 1$  is allowed for each of the fine structure components. Center: Magnification of the 2S–4P<sub>1/2</sub> resonance together with a fitted Lorentzian (dashed) that cannot be distinguished from the full line shape model unless one plots the fitting residuals at the bottom. Note that these residuals are well characterized by the last dispersive term in (40). The remaining deviations are very symmetric about  $\delta = 0$  and give rise to only a very small line pulling.

(34). **Figure 7** shows an example and illustrates that quantum interference adds to zero if all spherical components are detected with equal sensitivity as proven above. Another way to cancel the cross terms would be to add signals detected along the x-, y-, and z-axes (right side of Figure 7). This cancellation is independent of laser polarization. Yet another possibility is to align for the “magic angle” as introduced in this context by R.C. Brown et al.<sup>[16]</sup> It is easy to verify that the cross terms cancel each other in (44) for  $\theta = \arccos(1/\sqrt{3}) = 54.74^\circ$ . However, it should be noted that these strategies of using point-like detectors are not optimal in terms of signal collection efficiency.

We can now switch the role of the two line components and treat the 2S–4P<sub>1/2</sub> transition as a perturbation of the 2S–4P<sub>3/2</sub> transition. One may again compute the sum (34) or simply replace  $\delta \rightarrow \delta + \Delta$  and the relative intensities in (44):

$$I_{p=0}^{P_{3/2}}(\theta) \propto \left| \frac{1}{\delta + i\Gamma/2} - \frac{1}{\delta + \Delta + i\Gamma/2} \right|^2 (1 + \cos^2(\theta)) + \left| \frac{2}{\delta + i\Gamma/2} + \frac{1}{\delta + \Delta + i\Gamma/2} \right|^2 \sin^2(\theta) \quad (45)$$

#### 4.2.2. Expanded Line Shape

The expanded line shapes of the 2S–4P transitions can be either determined from (40)–(43) or in a simpler way with (8). Expanding (44) and (45) as (40), one obtains fairly simple expressions:

$$4P_{1/2}: \quad a_1 = 2 \quad a_2 = \frac{7 - 3 \cos(2\theta)}{\Delta^3} \quad a_4 = \frac{1 + 3 \cos(2\theta)}{\Delta} \quad (46)$$

$$4P_{3/2}: \quad a_1 = \frac{7}{2} - \frac{3}{2} \cos(2\theta) \quad a_2 = -\frac{4}{\Delta^3} \quad a_4 = -\frac{1 + 3 \cos(2\theta)}{\Delta} \quad (47)$$

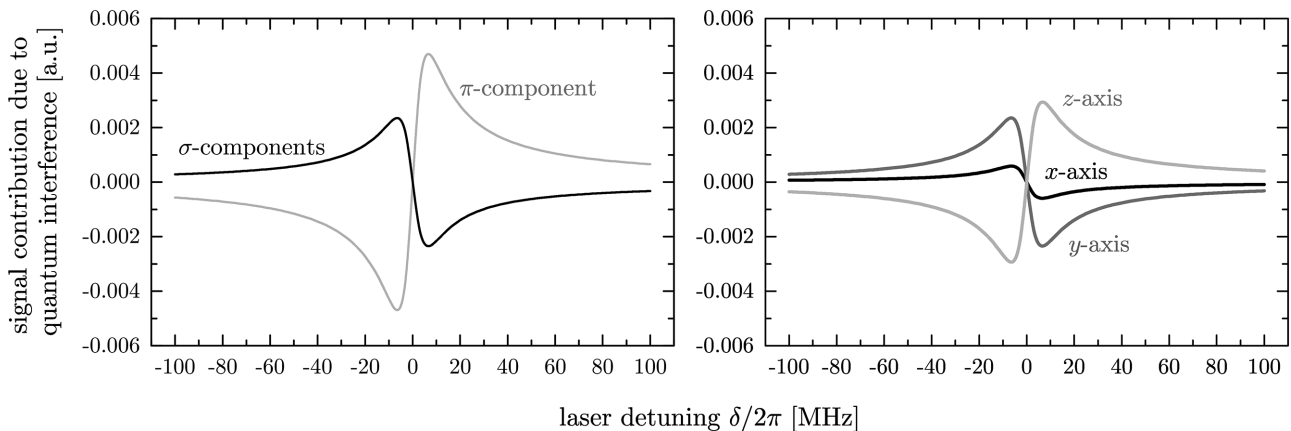


**Figure 7.** Left: Quantum interference contribution to the 2S–4P<sub>1/2</sub> resonance for linear laser polarization along the z-axis with the same relative units as in Figure 6. The emitted spherical components  $q = -1, 0, 1$  correspond to the  $\sigma^-$ ,  $\pi$ , and  $\sigma^+$  components. The  $\sigma$ -components have the same intensity pattern. Right: The same for linear laser polarization tilted by  $\theta_L = 30^\circ$  from the z-axis toward the x-axis. Signal detected with both polarizations along the x-, y-, and z-axes. These line distorting contributions add to zero independent of laser polarization.

In both cases, we recover the “magic angle” as a condition for  $a_4 = 0$ . Using (9) as the definition of the line pulling we get in leading order ( $\Delta \gg \Gamma$ )  $\Delta\omega \approx a_4/4a_1$ :

$$\Delta\omega(P_{1/2}) \approx \frac{1 + 3 \cos(2\theta)}{8} \frac{\Gamma^2}{\Delta} \quad (48a)$$

$$\Delta\omega(P_{3/2}) \approx -\frac{1 + 3 \cos(2\theta)}{14 - 6 \cos(2\theta)} \frac{\Gamma^2}{\Delta} \quad (48b)$$

This line shape may then be convoluted with a Gaussian to obtain a Fano–Voigt line shape (13) to take a possible Doppler broadening into account. An important feature of the expanded line shape is that it will always be of this form, not only for linear laser polarization. Without external fields, there are only two energy denominators such that the full line shape is the square modulus of the sum of two Lorentzians only. Another important property is that the line pulling does not average out by varying the detection angle  $\theta$ , say by rotating the laser polarization with a fixed detector position. At the same time (48a) and (48b) open up another, very powerful way of cancelling out the quantum interference by using the averaged line pullings of the 2S–4P<sub>1/2</sub> and the 2S–4P<sub>3/2</sub>, weighted by their leading-order line strength  $a_1$ . Note that for the 2S–4P<sub>3/2</sub>, this line strength depends on the observation direction. This so-called fine structure centroid is pulled through the quantum interference in next order by

$$\Delta\omega(\text{centroid}) \approx \frac{3 \sin(\theta)^2}{22 - 6 \cos(2\theta)} \frac{\Gamma^4}{\Delta^3} \approx 0 \quad (49)$$

It contributes with 1.2 Hz to the 2S–4P transition frequency at maximum, an accuracy level currently out of reach. However, approximations made, like neglecting saturation effects, can spoil this cancellation already on the level of 100 Hz for typical experimental parameters. Repeating the analysis with the other two laser spherical components,  $p = \pm 1$  yields different expressions for the line shapes but the same results for the line pullings (48a), (48b) and (49). This means the cancellation of the quantum interference induced line distortions takes place for any laser polarization. Since the compensation works for any angle  $\theta$ , it also works for a range of angles, that is, for any finite detection solid angle  $\Omega_d$ . We have used all of the cancellation schemes discussed in this work simultaneously, that is, modeling, large  $\Omega_d$ , and weighted average for our recent measurement of the 2S–4P centroid.<sup>[6]</sup>

#### 4.2.3. Comparison with Experimental Data

Line pulling due to quantum interference was clearly observed in our 2S–4P spectroscopy of atomic hydrogen. This became possible after carefully compensating other systematic effects. The largest one was the Doppler effect that was compensated with a standing wave excitation with 486 nm laser light delivered by a polarization-maintaining fiber and a high-quality collimator crossing the atomic beam at  $\approx 90^\circ$ .<sup>[27]</sup> Using a time-of-flight detection method, we could verify this method down to an uncertainty of 2.1 kHz. While the Doppler *shift* is compensated, the

Doppler broadening is not. Therefore, the Fano–Voigt line shape (13) was used for the data analysis.

Large-area photodetectors covering different directions were employed to record the fluorescence via the 4P–1S decay at 97 nm. The detection solid angles could not be determined with sufficient accuracy because of an unknown spatial dependence of the quantum efficiency. While the full line shapes (44) and (45) depend on the detection solid angle, the form of the expansion only depends on the number of resonances. Hence, by using as a fit function (40) or (13), the unknown geometry is modeled with only one additional parameter that measures the relative strength of the dispersive component.

To verify our line shape model in this way, it was much simpler to rotate the linear laser polarization than to move the detectors. **Figure 8** shows the observed line pulling together with the model with and without taking into account the quantum interference. To model the line pulling, we have to take the finite detection solid angle into account. To this end, we introduce three adjustable parameters, one amplitude to (46) and (47) and a variable coefficient of the cosine term in the denominator of (47). This model is shown as the gray curves in the upper part of **Figure 8**. As expected, the line pulling repeats with rotating the laser polarization with  $180^\circ$  and has the opposite sign for the two line components. On the other hand, no such modeling is necessary when using the Fano–Voigt profile as the line shape model (lower part of **Figure 8**). This removes the effects of quantum interference induced line pulling within a residual uncertainty of 0.2 kHz for the fine structure centroid.<sup>[6]</sup>

### 4.3. The Helium Triplet Fine Structure

One of the best probes to determine the value of the fine structure constant  $\alpha$  is to measure the  $g$ -factor of a single trapped electron<sup>[7]</sup> and compare the results with theoretical predictions. Very much like the case of hydrogen, this does not test the underlying theory of QED. One needs additional measurements to check for consistency. Another way to determine  $\alpha$  is using the Rydberg constant  $R_\infty = \alpha^2 m_e c / 2h$  from hydrogen spectroscopy and combine it with a value for  $m_e / h$  from atomic recoil measurements.<sup>[8,9]</sup> Also here, the current most precise values of  $\alpha$  disagree by 2.4 combined standard deviations.<sup>[8,52]</sup>

The fine structure of atoms provides another independent probe to the fine structure constant that has been proposed a long time ago<sup>[53]</sup> and used for that purpose extensively. Measured in atomic units, this splitting is proportional to  $\alpha^2$ , in contrast to the gross structure of atomic hydrogen that is in first and second order independent of  $\alpha$ . The fine structure of atomic hydrogen, that gave this constant its name, is not necessarily the best system for its determination. The  $n = 2$  triplet levels of helium have a larger splitting, a significantly smaller line width and are accessible with standard laser technology. Significant effort has been invested into the theory<sup>[54]</sup> to be compared with experimental results. When using  $^4\text{He}$ , no hyperfine structure complicates the level scheme that is shown at the left side of **Figure 9**. The 2<sup>3</sup>S level is metastable with a lifetime of 7900 s such that this state effectively acts as the ground state in many experiments.

There are several experimental approaches to measure the fine structure intervals. The latest work uses a variant of the Ramsey

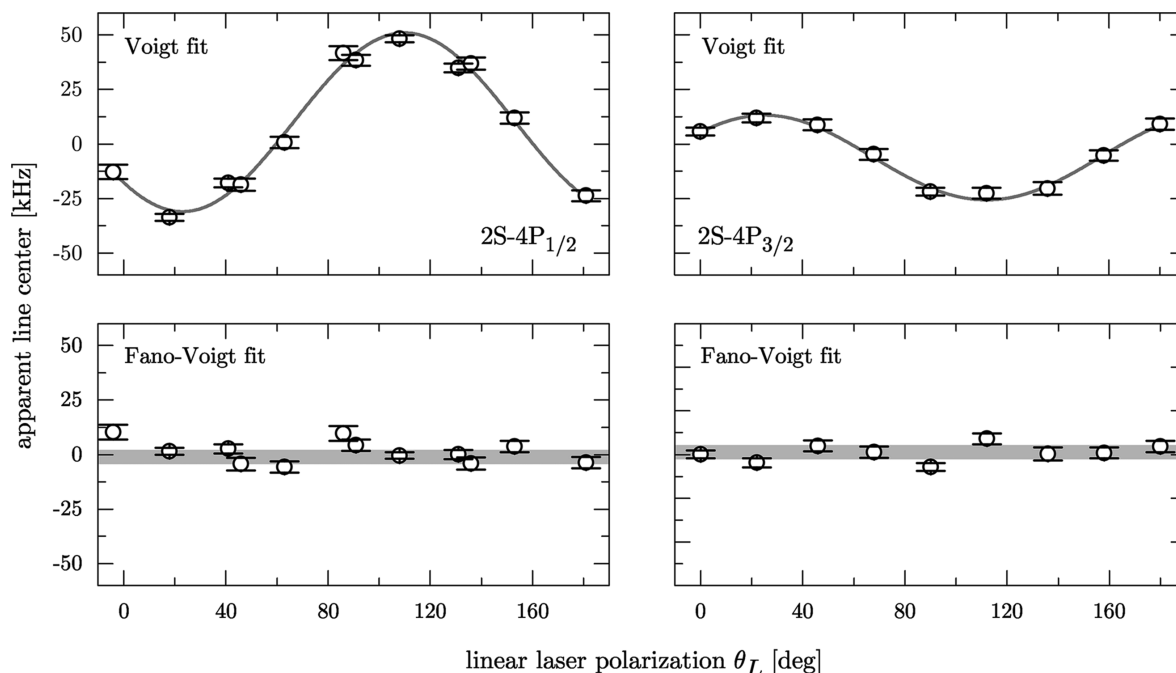


**Figure 8.** Example of the observed line pulling (relative to the results in ref. [6]) of the  $2S-4P_{1/2}$  and  $2S-4P_{3/2}$  resonances in atomic hydrogen due to quantum interference for laser excitation with linear polarization along  $\theta_L$  with respect to the z-axis. Top: When fitting a Voigt profile to the experimental lines the observed line pulling reaches up to 40 kHz. It is somewhat reduced from the maximum value by use of large solid angle photodetectors. Fitted sinusoidal functions of the type (46) and (47) demonstrate that the apparent line pulling is of that form. However, in practice neither the offset, the phase, nor the amplitude of this function is known because the solid angle and the position of the detector is experimentally difficult to access and the absolute frequency of the transition not known before the fit. Bottom: These problems have been avoided by using the Fano–Voigt line shape (13) to find the line center. The line pulling is reduced to the noise level, given by the residual first-order Doppler shift. The horizontal bars depict the final uncertainties, including systematic uncertainties. It should be added that this effect can not explain the “proton radius puzzle” (see ref. [6] for details).

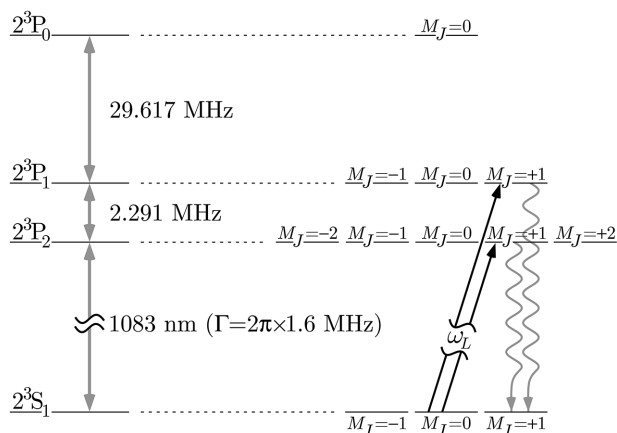


**Figure 9.** Level scheme of the  $^4\text{He } n = 2$  triplet system. Left: The fine structure splitting of the P states. Since the nucleus has no spin, no hyperfine structure is present. Right: Zeeman components that are probed with a circularly polarized laser, labeled  $\omega_L$ . Two possible transitions that are subject to mutual line pulling due to quantum interference are shown. The signal is obtained by laser induced repopulation of the  $2^3S_1 (M_J = 1)$  level.

method to drive the radio frequency transitions between the  $2^3P_J$  levels directly.<sup>[55]</sup> The other option is to measure at least two  $2^3S_1-2^3P_J$  transitions and determine the level splitting by computing the difference.<sup>[56]</sup> Saturation spectroscopy is another method<sup>[11,12]</sup>

that goes beyond the perturbative treatment here and comes with other systematic effects like velocity changing optical recoils.<sup>[29]</sup>

As an example we discuss Rabi-type spectroscopy that has been employed with a crossed atomic beam that is prepared in the initial  $2^3S (M_J = 0)$  level using a Stern–Gerlach filter.<sup>[10,57]</sup> The signal is generated by detecting atoms in the  $2^3S (M_J = 1)$  state after a second Stern–Gerlach filter (see right-hand side of Figure 9). Quantum interference takes place without interference of the emitted light as suggested by the classical toy model. Detection of the  $2^3S (M_J = 1)$  level is completely equivalent to observing only the  $\pi$  component of the emission. This probably justifies the term quantum interference. By switching quickly between the  $J = 2$  and  $J = 1$  components, severe systematic effects, like the Doppler effect, are cancelled. However, the mutual line pulling due to quantum interference is not. As these pullings have the opposite sign, it adds to the difference. This effect can be described in full by solving the optical Bloch equations<sup>[58]</sup> or with the explicit perturbative line shapes given in this work.

Detecting the final state instead of the fluorescence means that we can simply evaluate the scattering cross section (20) or (22) with the matrix elements (18) to obtain the line shape function:

$$I(\omega_L) \propto \left| \sum_{\epsilon} \sum_p (-1)^p S_{q,p}^{\epsilon, i \rightarrow f} \epsilon_{-p} \right|^2 \quad (50)$$

We do not have to worry about the detection geometry of the emitted light. In a sense, it is as if we detect the particular spherical

component, the  $\pi$  component in this case, within a solid angle of  $4\pi$ . The initial and final state are given by  $J_i = 1$ ,  $M_i = 0$ ,  $L_i = 0$  and  $J_f = 1$ ,  $M_f = 1$ ,  $L_f = 0$ , respectively. There are two excited states  $J_{e'} = 2$ ,  $M_{e'} = 1$ ,  $L_{e'} = 1$  and  $J_{e''} = 1$ ,  $M_{e''} = 1$ ,  $L_{e''} = 1$  that are separated by  $\Delta = 2\pi \times 2.291$  GHz. To compute the matrix elements we could use (28) with the nuclear spin set to zero, or instead use the corresponding expression without hyperfine structure

$$d_q(e \rightarrow f) = (-1)^{J_f - M_f} \begin{pmatrix} J_f & 1 & J_e \\ -M_f & q & M_e \end{pmatrix} \langle n_f, L_f || d || n_e, L_e \rangle \times (-1)^{L_f + S + J_e + 1} \sqrt{(2J_f + 1)(2J_e + 1)} \begin{Bmatrix} L_f & J_f & S \\ J_e & L_e & 1 \end{Bmatrix} \quad (51)$$

and an analogous expression for the absorbing dipole moment that is obtained by replacing  $f \rightarrow e$ ,  $e \rightarrow i$ , and  $q \rightarrow p$ . We assume circularly polarized light with  $p = 1$  and detect only the decay channel  $q = 0$ . With this the explicit line shape is obtained as

$$I_{q=0, p=1} \propto \left| \frac{1}{\delta + i\Gamma/2} - \frac{1}{\delta \pm \Delta + i\Gamma/2} \right|^2 \approx \frac{1}{\delta^2 + (\Gamma/2)^2} \mp \frac{2\delta/\Delta}{\delta^2 + (\Gamma/2)^2} \quad (52)$$

where the  $-$  sign describes the line pulling of the  $2^3S_1-2^3P_2$  transition by the  $2^3S_1-2^3P_1$  transition and the  $+$  sign for the reverse case. The detuning  $\delta$  is measured relative to the  $2^3S_1-2^3P_2$  energy splitting. The last expression is the expanded line shape that can be obtained either with the full model (40)–(43) or, in a simpler way, with the classical toy model (8). If required, the latter may be convoluted with a Gaussian to account for a possible Doppler broadening to obtain a Fano–Voigt line shape (13).

For the line pulling of the fine structure interval, the line pullings of the two optical transitions, that are given by (9), add. Since  $\Delta/\Gamma = 1400$ , only the coefficients  $a_1 = 1$  and  $a_4 = \mp 2/\Delta$  need to be taken into account, and they can be extracted from (52) or (41) and (43). This yields the pulling of the  $2^3P_2-2^3P_1$  fine structure interval:

$$\Delta\omega \approx -2\pi \times \frac{\Gamma^2}{\Delta} = -2\pi \times 1.1 \text{ kHz} \quad (53)$$

In other words, the two lines appear to be closer by 1.1 kHz if the two measured optical resonances are fitted with a Lorentzian line shape instead of the full line shape (43). This result is in good agreement with a  $-1.2(0.1)$  kHz line pulling obtained from the full-fledged optical Bloch equations.<sup>[58]</sup>

Large discrepancies between measurements of the helium triplet fine structure are found in the literature. For example, X. Zheng et al.<sup>[59]</sup> find their result for the  $2^3S-2^3P$  centroid-off by 20 combined standard deviations from the result of P. Cancio Pastor.<sup>[60]</sup> Correcting components of the latter for the neglected quantum interference gives a significantly larger error bar.<sup>[61]</sup> Signals from saturation spectroscopy are even more difficult to understand when it comes to tiny line shape distortions. These, and many other line-distorting effects need to be under full control,

when important precision data can only be obtained from broad transitions.

## Acknowledgements

T.W.H. acknowledges support from the Max Planck Foundation. N.K. acknowledges support from DFG-RFBR grants (HA 1457/12-1 and 17-52-12016) and A.M. was supported by the Deutsche Forschungsgemeinschaft (DFG, German Research Foundation) - Project number 390524307. This article is part of the Special Issue on *The Revised SI: Fundamental Constants, Basic Physics and Units*, highlighting the revision and redefinition of the International System of Units (SI) to come into effect in May 2019.

## Conflict of Interest

The authors declare no conflict of interest.

## Keywords

high resolution laser spectroscopy, proton charge radius, quantum interference, rydberg constant, testing quantum electrodynamics

Received: January 28, 2019

Revised: March 12, 2019

Published online:

- [1] D. B. Newell, F. Cabiati, J. Fischer, K. Fujii, S. G. Karshenboim, H. S. Margolis, E. de Mirandés, P. J. Mohr, F. Nez, K. Pachucki, T. J. Quinn, B. N. Taylor, M. Wang, B. M. Wood, Z. Zhang, *Metrologia* **2018**, 55, L13.
- [2] The kg, for example, is realized within the new SI system by fixing Planck's constant and using a Watt balance that employs the quantum Hall effect, the Josephson effect, and a velocity measurement. The latter two use the SI second and a fixed value for the speed of light for the length measurement.
- [3] P. Gill, *J. of Phys.: Conf. Ser.* **2016**, 723, 012053.
- [4] G. Leuchs, L. L. Sánchez-Soto, *Eur. Phys. J. D* **2013**, 67, 57.
- [5] T. Udem, *Nat. Phys.* **2018**, 14, 632.
- [6] A. Beyer, L. Maisenbacher, A. Matveev, R. Pohl, K. Khabarova, A. Grinin, T. Lamour, D. C. Yost, T. W. Hänsch, N. Kolachevsky, T. Udem, *Science* **2017**, 358, 79.
- [7] G. Gabrielse, D. Hanneke, T. Kinoshita, M. Nio, B. Odom, *Phys. Rev. Lett.* **2006**, 97, 030802.
- [8] R. H. Parker, C. Yu, W. Zhong, B. Estey, H. Müller, *Science* **2018**, 360, 191.
- [9] J. Fernandez, A. J. Garcia-Adeva, R. Balda, *Phys. Rev. Lett.* **2006**, 97, 033001.
- [10] J. Castilleja, D. Livingston, A. Sanders, D. Shiner, *Phys. Rev. Lett.* **2000**, 84, 4321.
- [11] G. Giusfredi, P. C. Pastor, P. D. Natale, D. Mazzotti, C. de Mauro, L. Fallani, G. Hagel, V. Krachmalnicoff, M. Inguscio, *Can. J. Phys.* **2005**, 83, 301.
- [12] T. Zelevinsky, D. Farkas, G. Gabrielse, *Phys. Rev. Lett.* **2005**, 95, 203001.
- [13] J. S. Borbely, M. C. George, L. D. Lombardi, M. Weel, D. W. Fitzakerley, E. A. Hessels, *Phys. Rev. A* **2009**, 79, 060503.
- [14] F. Low, *Phys. Rev.* **1952**, 88, 53.
- [15] M. Horbatsch, E. A. Hessels, *Phys. Rev. A* **2010**, 82, 052519.

- [16] R. C. Brown, S. Wu, J. V. Porto, C. J. Sansonetti, C. E. Simien, S. M. Brewer, J. N. Tan, J. D. Gillaspay, *Phys. Rev. A* **2013**, *87*, 032504.
- [17] B. W. Holmes, J. A. R. Griffith, *J. Phys B* **1995**, *28*, 191.
- [18] U. D. Jentschura, P. J. Mohr, *Can. J. Phys.* **2002**, *80*, 633.
- [19] L. Allen, J. H. Eberly, *Optical Response and Two-level Atoms*, Dover, New York **1987**.
- [20] H. J. Metcalf, P. van der Straten, *Laser Cooling and Trapping*, Springer, Berlin **2002**.
- [21] S. Haroche, *Top. Appl. Phys.* **1972**, *13*, 253.
- [22] A. Ozawa, J. Davila-Rodriguez, J. R. Bounds, H. A. Schuessler, T. W. Hänsch, T. Udem, *Nat. Commun.* **2017**, *8*, 1.
- [23] D. C. Yost, A. Matveev, E. Peters, A. Beyer, T. W. Hänsch, T. Udem, *Phys. Rev. A* **2014**, *90*, 012512.
- [24] H. Fleurbaey, F. Biraben, L. Julien, J. P. Karr, F. Nez, *Phys. Rev. A* **2017**, *95*, 052503.
- [25] U. Fano, *Phys. Rev.* **1961**, *124*, 1866.
- [26] B. de Beauvoir, F. Nez, L. Julien, B. Cagnac, F. Biraben, D. Touahri, L. Hilico, O. Acef, A. Clairon, J. J. Zondy, *Phys. Rev. Lett.* **1997**, *78*, 440.
- [27] A. Beyer, L. Maisenbacher, A. Matveev, R. Pohl, K. Khabarova, Y. Chang, A. Grinin, T. Lamour, T. Shi, D. C. Yost, T. Udem, T. W. Hänsch, N. Kolachevsky, *Opt. Expr.* **2016**, *24*, 17470.
- [28] A. Beyer, J. Alnis, K. Khabarova, A. Matveev, C. G. Parthey, D. C. Yost, R. Pohl, T. Udem, T. W. Hänsch, N. Kolachevsky, *Ann. d. Phys.* **2013**, *525*, 671.
- [29] F. Minardi, M. Artoni, P. Cancio, M. Inguscio, G. Giusfredi, I. Carusotto, *Phys. Rev. A* **1999**, *60*, 4164.
- [30] S. Schippers, *Int. Rev. At. Mol. Phys.* **2011**, *2*, 151.
- [31] M. Abramowitz, I. Stegun, *Handbook of Mathematical Functions with Formulas, Graphs, and Mathematical Tables*, Dover, New York **1972**.
- [32] W. Gautschi, *SIAM J. Num. Anal.* **1970**, *7*, 187.
- [33] Z. Ficek, S. Swain, *Quantum Interference and Coherence*, Springer, Berlin **2005**.
- [34] A. A. Buchheit, G. Morigi, *Phys. Rev. A* **2016**, *94*, 042111.
- [35] D. A. Cardimona, C. R. Stroud, *Phys. Rev. A* **1983**, *27*, 2456.
- [36] D. A. Cardimona, M. G. Raymer, C. R. Stroud, *J. Phys. B* **1982**, *15*, 55.
- [37] S.-Y. Zhu, M. O. Scully, *Phys. Rev. Lett.* **1996**, *76*, 388.
- [38] R. Loudon, *The Quantum Theory of Light*, Oxford University Press, New York **2000**.
- [39] It should be noted, that within this semiclassical picture, it is actually not exact to speak about photons but convenient.
- [40] I. I. Sobelman, *Atomic Spectra and Radiative Transitions*, Springer, Berlin **1979**.
- [41] R. C. Hilborn, *Am. J. Phys.* **1982**, *50*, 982.
- [42] H. A. Bethe, E. E. Salpeter, *Quantum Mechanics of One- And Two-Electron Atoms*, Dover, New York **1957**.
- [43] A. Messiah, *Quantum Mechanics*, Vol. 2. Appendix C.I and C.II, Amsterdam, The Netherlands **1975**.
- [44] Not to be confused with the spherical components introduced before.
- [45] Note that at the detection point, the polarization of the  $q = \pm 1\sigma$  components can be anything between linear and circular.
- [46] S. R. Lundeen, F. M. Pipkin, *Phys. Rev. Lett.* **1981**, *46*, 232.
- [47] A. Marsman, M. Horbatsch, Z. A. Coriveau, E. A. Hessels, *Phys. Rev. A* **2018**, *98*, 012509.
- [48] A. Antognini, F. Nez, K. Schuhmann, F. D. Amaro, F. Biraben, J. M. R. Cardoso, D. S. Covita, A. Dax, S. Dhawan, M. Diepold, L. M. P. Fernandes, A. Giesen, A. L. Gouvea, T. Graf, T. W. Hänsch, P. Indelicato, L. Julien, C.-Y. Kao, P. Knowles, F. Kottmann, E.-O. Le Bigot, Y.-W. Liu, J. A. M. Lopes, L. Ludhova, C. M. B. Monteiro, F. Mulhauser, T. Nebel, P. Rabinowitz, J. M. F. dos Santos, L. A. Schaller, C. Schwob, D. Taqqu, J. F. C. A. Veloso, J. Vogelsang, R. Pohl, *Science* **2013**, *339*, 417.
- [49] That is, with low sensitivity to external fields.
- [50] D. J. Berkeland, E. A. Hinds, M. G. Boshier, *Phys. Rev. Lett.* **1995**, *75*, 2470.
- [51] A computer algebra system has been used for that purpose.
- [52] T. Aoyama, M. Hayakawa, T. Kinoshita, M. Nio, *Phys. Rev. D* **2015**, *91*, 033006 and erratum *Phys. Rev. D* **2017**, *96*, 019901(E).
- [53] C. Schwartz, *Phys. Rev.* **1964**, *134*, A1181.
- [54] K. Pachucki, V. Patkóš, V. Yerokhin, *Phys. Rev. A* **2017**, *95*, 062510.
- [55] K. Kato, T. D. G. Skinner, E. A. Hessels, *Phys. Rev. Lett.* **2018**, *121*, 143002.
- [56] X. Zheng, Y. R. Sun, J. J. Chen, W. Jiang, K. Pachucki, S. M. Hu, *Phys. Rev. Lett.* **2017**, *118*, 063001.
- [57] M. Smiciklas, D. Shiner, *Phys. Rev. Lett.* **2010**, *105*, 123001.
- [58] A. Marsman, M. Horbatsch, E. A. Hessels, *Phys. Rev. A* **2012**, *86*, 040501.
- [59] X. Zheng, Y. R. Sun, J. J. Chen, W. Jiang, K. Pachucki, S. M. Hu, *Phys. Rev. Lett.* **2017**, *118*, 063002.
- [60] P. Cancio Pastor, G. Giusfredi, P. De Natale, G. Hagel, C. de Mauro, M. Inguscio, *Phys. Rev. Lett.* **2004**, *92*, 023001 and erratum **2006**, *97*, 139903(E).
- [61] A. Marsman, M. Horbatsch, E. A. Hessels, *J. Phys. Chem. Ref. Data* **2015**, *44*, 031207.